# Machining of Additively Manufactured Titanium Ti-6Al-4V; Cutting Forces and Chip Morphology

by

Nam Nguyen

A thesis submitted to the School of Graduate and Postdoctoral Studies in partial fulfillment of the requirements for the degree of

**Master of Applied Science in Mechanical Engineering**

Faculty of Engineering and Applied Science
University of Ontario Institute of Technology
(Ontario Tech University)
Oshawa, Ontario, Canada
April 2023

# Thesis Examination Information

Submitted by:
**Nam Nguyen**

## Master of Applied Science in Mechanical Engineering

Thesis title:
## Machining of Additively Manufactured Titanium Ti-6Al-4V; Cutting Forces and Chip Morphology

An oral defense of this thesis took place on April 12th, 2023 in front of the following examining committee:

**Examining Committee**

| | |
|---|---|
| Chair of Examining Committee | Dr. Ghaus Rizvi |
| Research Supervisor | Dr. Sayyed Ali Hosseini |
| Examining Committee Member | Dr. Hossam Kishawy |
| Thesis Examiner | Dr. Brendan MacDonald |

The above committee determined that the thesis is acceptable in form and content and that a satisfactory knowledge of the field covered by the thesis was demonstrated by the candidate during an oral examination. A signed copy of the Certificate of Approval is available from the School of Graduate and Postdoctoral Studies.

## Author's Declaration

I declare that the thesis presented here is my original work that I have authored. It is a true copy of the thesis.

I grant Ontario Tech University the right to lend this thesis, for the purpose of scholarly research, to other individuals or institutions. Additionally, I grant Ontario Tech University the right to reproduce by means of photocopying or other, this thesis, partially or fully per the request of other institutions or individuals for the purpose of scholarly research. I acknowledge this thesis will be made publicly available through electronic means.

Nam Nguyen

# Abstract

This thesis studies the machining of additively manufactured (AM) titanium Ti-6Al-4V and presents a model to determine Johnson Cook (J-C) constitutive parameters from complex machining processes through numerical modeling and experimental validation. The J-C parameters are important in describing the characteristics and behaviors of materials during high-strain rate high-temperature machining processes. These parameters are traditionally determined through time-consuming and costly split-Hopkinson pressure bar tests. The proposed model uses a combination of experimentally measured cutting forces and optimization methods including genetic algorithm and particle swarm optimization to find the suitable J-C parameters. Force simulation and experiments were conducted to validate the proposed model and the results showed its effectiveness in estimating the J-C parameters directly from milling tests as an oblique cutting operation. Chip morphology has also been investigated to determine the mechanics of chip formation and its relationship to the properties of the AM titanium.

**Keywords: milling, additive manufacturing, Johnson-Cook model, Oxley model, genetic algorithm, particle swarm optimization, chip morphology**

# Acknowledgements

I want to express my immense appreciation to my research supervisors Dr. Sayyed Ali Hosseini for his endless support over the last two years. You have inspired me to work hard and strive to reach my fullest potential.

Sincere love and appreciation to my family for their endless support throughout my entire life and especially my time away in Canada.

I would also like to acknowledge Dylan Bender and Connor Hopkins for providing me with invaluable machining knowledge; and Benjamin Deboer for sharing his academic knowledge. Additionally, I would like to thank Peter Kahr from the Faculty of Engineering and Applied Science at Ontario Tech University for helping me to prepare materials and maintain the CNC milling machine.

# Statement of Contribution

Parts of the work described in this thesis is currently in the last proofing step or under conditional acceptance as follows:

**Section 4.2**

Published in the Journal of Manufacturing Processes

N. Nguyen and A. Hosseini, “Direct calculation of Johnson-Cook constitutive material parameters for oblique cutting operations,” *Journal of Manufacturing Processes*, vol. 92, pp. 226-237, 2023, doi: https://doi.org/10.1016/j.jmapro.2023.02.032.

**Section 4.3**

Published in CIRP Annals Journal of Manufacturing Technology

H.A. Kishawy, N. Nguyen, A. Hosseini and M. Elbestawi, “Machining characteristics of additively manufactured titanium, cutting mechanics and chip morphology,” *CIRP Annals - Manufacturing Technology*, doi: https://doi.org/10.1016/j.cirp.2023.04.056.

# Table of Contents

# List of Figures

# List of Tables

# Chapter 1

# Introduction

## 1.1 Background

Metal Additive Manufacturing (AM), also known as metal 3D printing, is a process of creating three-dimensional (3D) metal parts by building them up layer by layer using a digital model. The process begins by creating a 3D model of the part using computer-aided design (CAD) software. This model is then divided into thin layers, and each layer is used as a profile for building the final part.

According to the standard set by American Society for Testing and Materials (ASTM), AM technologies fall into seven categories [5], namely Material Extrusion (ME), Powder Bed Fusion (PBF), Directed Energy Deposition (DED), Material Jetting (MJ), Binder Jetting (BJ), Vat Photopolymerization (VP), and Lamination.

ME is one of the most popular methods for end use plastic parts due to its low cost. In specific, Fused Filament Fabrication (FFF), as a subset of ME, is one of the common methods for AM of thermoplastic material where the polymer is melted and extruded through a nozzle to form a continuous filament, which is then built-up layer by layer to shape the final product. However, ME only made up 10% of the metal AM market in 2020 [6]. This is due to the many difficulties related to the sintering process of metal ME and its final part quality. Typically, metal ME starts with feedstock or filaments that contains metal powder suspended in sacrificial polymer binders [7]. The purpose of the binder is to loosely adheres the printed layers and lines during the printing process. After the printing process, the parts are still very fragile and need to be further processed to become fully dense metal parts. Some process requires additional washing and then sintering, others only require sintering. In any case, the sacrificial binder is washed or burned away [7]. Then the sintering process, metal powder slowly melts and fuses together to form a solid metal part. However, due to the sintering process, the part shrinks significantly, up to 20% in some cases [8]. Ideally, the shrinkage should be uniform, but this is typically not the case, resulting in warping and lowering dimensional accuracy. Too much warping will also lead to part breakage and print failure. This forces parts to be printed with lower infill percentage, limiting the possibility of large fully dense parts [8]. Furthermore, due to the exposed layer lines and printing lines, the surface quality of metal ME inherits the same issues from traditional polymer ME [9].

DED technologies cover 16% of the metal AM market and is grouped into two categories: cold spray and thermal energy [6]. Cold spray uses fine particles to create a dense coating, while thermal energy uses laser beams, electron beams, plasma, or arc to melt and add material to the build platform. Compared to metal PBF, despite its potential as an important parts repair method, metal DED showed much lower industry application due to its lack of reliability and repeatability. This deficit is due to the complex sensing and monitoring requirements of DED, both regarding hardware and software [10].

BJ is a technology that was used mainly for sand moulds application, but in recent years, its development has allowed for the printing of metal parts [11]. Similar to PBF, BJ uses a metal powder bed, but instead of using heat to immediately form parts, BJ uses liquid binder to form a temporary 3D part. The printing process involves spreading metal powder evenly across a build platform, then a print head dispenses droplets of liquid binder onto the powder. The binder droplets adhere the powder particles at specific locations based on the part model, forming a temporary green part. After the printing process is completed, the green part is then subjected to a sintering process, which removes the binder and fuses the powder particles together, creating a solid metal part. BJ is highly versatile, as it can be used to process a wide range of different materials. In addition, BJ build area does not require an airtight inert gas chamber like PBF. Thus, its build volumes are usually larger, making it well-suited for large-scale production. However, the sintering process also degrades the quality of the parts similar to ME, additional processing is required such as bronze infiltration [11], limiting its adoption.

MJ, also known as inkjet 3D printing, is a 3D printing process that uses piezo printing heads to deposit droplets of liquid photopolymers, which are then cured immediately at the printing location using ultraviolet lamps. This process is also capable of creating multi-material parts by selectively depositing multiple photo-curable polymer resins simultaneously. The inkjet 3D printing technology has been widely adopted for a variety of applications, including the production of prototypes, functional polymer components, custom anatomical models, and scaffolds for tissue engineering [12]. However, as there is no known metallic material in liquid form that can be solidified using light, MJ cannot be used to make metal parts.

VP process involves exposing photo-sensitive materials to controlled amounts of radiation or light. This method works by polymerizing the material in layers, which then combine to form a complete 3D object. VP can be used to process photopolymers and resins. There are several variations of VP, including Stereolithography, Digital Light Processing, Two-Photon Polymerization, and Volumetric 3D Printing [13]. VP has many applications in jewelry, dentals, medical and biomedical. However, similar to

MJ, VP relies on polymer resins that are stored in liquid form, then solidified during the printing process. Therefore, VP cannot be used to manufacture metal parts.

Metal sheet lamination, also known as laminated object manufacturing (LOM), is a manufacturing process that utilizes metal sheets as the raw material. The process involves using a localized energy source, such as ultrasonic or laser, to bond a stack of precisely cut metal sheets together to form a 3D object. The most common method used in metal sheet lamination is ultrasonic additive manufacturing (UAM) or ultrasonic consolidation. In UAM, ultrasonic waves and mechanical pressure are applied to the stack of metal sheets at room temperature, resulting in the bonding of the interfaces between the sheets through diffusion rather than melting. The metal sheets are bonded layer-by-layer until a complete 3D object is formed, all without the use of a heat source. Before the ultrasonic consolidation process, the metal sheets are typically cut to the desired geometry, and traditional polishing can be applied during or after the consolidation process to achieve a detailed finish [14]. There are many difficulties in regard to the LOM process, specifically, it is difficult to control the height of the part, as the layer thickness can change during the consolidation process under pressure. In addition, the accumulating direction shows lower mechanical properties compared to the other two directions. Part failure due to delamination is also a concern. These limits the industry adoption of LOM greatly, where LOM only accounts for 2% of metal AM market [6].

This thesis focuses on PBF, as it is currently the most widely used method for metal AM. Among the aforementioned AM methods, PBF dominates the market, accounting for 54% of the metal AM industry in 2020 [6]. PBF is similar to BJ, for every layer, a powder bed is evenly spread, metal powder is melted or sintered locally using a high-power laser or electron beam, which traces the pattern in each layer to create the final part. Once one layer is fused, the next layer of powder is spread, and the melting or sintering process repeats until the desired object is printed. The technology is widely used to produce complex geometries, functional prototypes, and end-use parts in various industries such as aerospace, medical, automotive, and tooling industry [15]. PBF is known for its ability to produce parts with intricate details and minimal waste, which is otherwise not possible to produce in one piece with traditional manufacturing methods.

There are currently many barriers hindering the widespread application of AM parts. One of the most important factors that limits the use of metal AM parts is relative lack of knowledge of material behavior. Firstly, the microstructure of AM parts can vary significantly by altering process parameters, which then affect the mechanical properties of the parts when compared to those of wrought metals. Secondly, properties can vary even within a single part due to the nature of the layer-by-layer build process. Thirdly, anisotropy which is more pronounced compared to wrought metals. As a result of anisotropy, the properties can vary depending on the direction of the build, which can make it more difficult to predict the properties of an AM metallic part. Finally, the properties of AM parts can also be affected by post-processing steps such as heat treatment, which can further complicate the determination of the material properties. In contrast, wrought metals are produced through more traditional manufacturing methods, such as casting, forging, or rolling, which results in a more homogeneous microstructure and more consistent properties. Therefore, material properties of wrought metals are readily available and well documented. There are also very detailed established guidelines for testing the non-AM metals which makes experimentation easier.

Material properties can be determined by performing mechanical or metallurgical testing. For instance, tensile tests can be used for obtaining yield strength, ultimate tensile strength, modulus of elasticity, ductility, and toughness, while indentation tests can be employed to measure the hardness, and cyclic loading tests will result in determining the fatigue life, etc. All of these testing methods are performed at relatively low deformation rate (low strain rate) and are referred to quasi-static tests. Thus, these properties can be easily obtained for AM metals. However, material properties are not only the function of material itself. They are being highly affected by other parameters such as strain rate and temperature. As a result, this thesis focuses on the testing methods for determining material properties, such as flow stress, in high strain rate and high temperature scenarios.

The typical method of obtaining the high strain rate and high temperature properties of metals is the Split-Hopkinson pressure bar test (SHPB). It is a type of impact testing in which a high-velocity impactor strikes the specimen and the resulting stress and strain in the specimen are measured, see Fig. 1.1. The SHPB test setup typically consists of a pair of metal bars, called pressure bars, that are arranged in a split configuration. One of the pressure bars is fixed and the other one is movable. The specimen is placed between the two bars and is struck by an impactor, which applies an impulsive force causing a high-strain rate deformation in the specimen. The deformation of the specimen is measured by strain gages placed on the pressure bars, and the stress-strain behavior of the material is determined from these measurements. Unfortunately, SHPB test has its own limitations. Firstly, the SHPB test requires a complex setup and specialized equipment, including high-speed data acquisition systems, strain gages, and impactors. This can make the test expensive and difficult to perform, due to the complexity and dangerous nature of the process, require shooting high speed projectiles through a tube [16]. More importantly, SHPB tests are typically limited to strain rates up to $10^3 - 10^4\ s^{-1}$ and relatively low temperatures [17]. This can make it difficult to obtain accurate results for materials that experience

Figure 1.1: Split-Hopkinson pressure bar test diagram.

large strain rates up to $10^6\ s^{-1}$ under loading and instantaneous heating, such as the ones typically experienced in machining processes [18]. The important question here is what the relevance of machining is, as a subtractive manufacturing (SM) process, to AM metals.

Hybrid manufacturing, an innovative approach combining AM and SM techniques, has garnered significant attention in advanced manufacturing. Implementation of machining in post-processing of AM metal components is crucial. While AM excels in fabricating intricate parts with complex geometries previously unachievable using traditional methods, AM-produced parts may exhibit inferior surface quality and dimensional accuracy compared to SM techniques, such as machining. This point is discussed further in Literature Review.

To address these limitations, SM can be employed to finish-machine critical surfaces on AM parts, such as mating surfaces, ensuring high dimensional accuracy and facilitating precise assembly. Furthermore, SM plays an essential role in optimizing the performance of AM-produced components, such as turbine blades. These parts often require weight balancing through machining to guarantee operational stability and reliability in high-speed applications. Overall, the synergistic combination of AM and SM processes in hybrid manufacturing paves the way for producing highly complex, accurate, and functional metal components across a wide array of industries.

## 1.2 Literature Review

### 1.2.1 Additive Manufactured Metals and Finish Machining

AM metals has becoming increasingly popular in recent years due to the drastic improvement in metal printing technology. However, in addition to the previously mentioned concerns regarding their mechanical properties, there are also major concerns about the achievable dimensional accuracy and surface quality of as printed AM metals. These issues are more pronounced in AM of complex geometries with overhang surfaces and support structures. Removal of the support structure negatively impacts the workpiece surface and jeopardizes the fatigue resistance, which is very sensitive to surface quality [19].

Employing a hybrid of AM and machining, as a subtractive manufacturing (SM), successfully combines the design and manufacturing flexibility of AM with high surface quality and dimensional accuracy attainable from machining. However, machining AM metals is not a straightforward job. AM metal parts show different machinability characteristics as compared to their wrought metal counterparts [20]. In addition, these parts are typically made of high-performance metals, e.g., titanium or superalloys, which are notoriously difficult-to-cut and include complex features that make them a lot less rigid than their regular counterparts and thus difficult to fixture [21]. As a result, thorough understanding of cutting mechanics and accurate prediction of machining forces is an imminent need to avoid chatter and achieve a high-quality product.

Some researchers have investigated the machinability of AM metals, specifically focusing on their higher hardness, yield strength, and ultimate tensile strength compared to wrought metals. It has been shown that machining AM metals typically results in higher cutting forces and tool wear [22, 23]. Guo et al. [22] conducted machining test on AISI 316L stainless steel AM parts made from high-power direct laser deposition (HP DLD). They found that machining forces along the build direction of 0° is higher than along 90°. They attributed this to the higher hardness along 0° causing higher tool wear. Rotella et al. [20] compared the surface roughness of machined titanium Ti-6Al-4V parts made from electron beam melting (EBM) and direct metal laser sintering (DMLS) AM methods versus wrought. For the same feeds and speeds, the roughness of the finish machined wrought part is the lowest, followed by finish machined EBM and then DMLS. They attributed this difference to the lower ductility exhibited by the AM samples. They also suggested that optimized cutting parameters for wrought titanium is not optimized for AM titanium.

In addition, studying the mechanics of chip formation when machining AM titanium alloys revealed that adiabatic shear banding and resultant saw-toothed chip were still present similar to that of wrought titanium [23, 24]. However, no detailed model has been proposed to predict cutting forces during the machining of AM metals. Also, the possible differences between mechanics of chip formation when machining AM and wrought metal has not yet been thoroughly investigated.

### 1.2.2 Material Models

In order to simulate the material behavior during any manufacturing process, including machining, a reliable model that describes the way material reacts to forces, strains, strain-rates, and temperature is a key element. There are different material models available such as the Zerilli-Armstrong (Z-A) model [25], Kocks–Mecking–Estrin (KME) model [26], and Johnson-Cook (J-C) model [27]. The Z-A model is a constitutive model that relates strain, strain rate, and temperature to flow stress, as shown in Eq. 1.1.

$$\sigma = \left(C_1 + C_2\epsilon^n\right)\exp\left[-\left(C_3 + C_4\epsilon\right)T^* + \left(C_5 + C_6T^*\right)\ln\dot{\epsilon}^*\right] \tag{1.1}$$

In Eq. 1.1, $C_1$ to $C_6$, and $n$ are material constants, $T^*$ is temperature modifier defined by $T^* = T - T_{ref}$, $T_{ref}$ is the reference temperature or room temperature, and $\dot{\epsilon^*}$ is the strain rate modifier expressed by $\dot{\epsilon^*} = \dot{\epsilon}/\epsilon_0$, where $\epsilon_0$ is the quasi-static reference strain rate.

The KME model is another constitutive model used to describe the nonlinear strain hardening behavior of materials, particularly metals. The basic KME model, as shown in Eq. 1.2, does not account for elevated temperature, however some modified KME models can include affect of temperature on flow stress [22]. In Eq. 1.2, $\sigma_0$ is the frictional stress, $M$ is the Taylor factor, $\alpha$ is a constant, $\mu$ is the shear modulus, $b$ is the burgers vector, and $\rho$ is the dislocation density.

$$\sigma = [\sigma_0 + M\alpha\mu b\sqrt{\rho}]\left(\frac{\dot{\epsilon}}{\dot{\epsilon_0}}\right)^{(1/m)} \tag{1.2}$$

The J-C model is also a constitutive material model used for predicting flow stress in metals subjected to rapid (high strain rate) deformation considering the effect of temperature. It is the most widely used one among the aforementioned models. J-C model has many advantages; it is relatively simple and easy to use, requiring a smaller number of parameters that can be determined from experiments or simulations. It can be applied to a wide range of materials and can be used for both tensile and compressive loading conditions. The J-C model is an empirical model, which is built upon experimental data. It is a combination of three different terms that describe the effect of strain, strain rate, and temperature on flow stress, as shown in Eq. 1.3.

$$\sigma = (A + B\epsilon^n)\left[1 + C\ln\left(\frac{\dot{\epsilon}}{\dot{\epsilon_0}}\right)\right]\left[1 - \left(\frac{T - T_r}{T_m - T_r}\right)^m\right] \tag{1.3}$$

The first term of the J-C equation describes the effect of strain on flow stress using yield stress ($A$), strength coefficient ($B$), and strain sensitivity exponent ($n$). The second term represents the effect of strain rate using strain rate sensitivity constant ($C$) multiplied by the natural logarithm of the normalized strain rate ratio, where the reference quasi-static strain rate is typically $\dot{\epsilon_0} = 1\,s^{-1}$. The third term expresses the effect of thermal softening, where $T$ is the current temperature of the material, $T_r$ is the reference/room temperature, and $T_m$ is the melting point of the material. As strain rate increases, the flow stress required to deform the material increases. In contrast, as the material heats up, flow stress decreases until it reaches zero when $T$

reaches $T_m$. For this thesis, the J-C model was chosen as the material model for flow stress calculation within the extended Oxley model. Despite not taking into account the effect of strain softening, the J-C model is still the most popular model used in cutting process simulation [28].

### 1.2.3 Methods of Obtaining Johnson-Cook Parameters

Extracting J-C parameters from the machining process itself is a promising method to overcome the difficulty of high strain rate and high temperature tests e.g., SHPB. Numerous mechanical testing methods were proposed to be used as alternative to SHPB tests. In 1997, Rule [29] used Taylor impact tests and gradient based optimizer to search for J-C parameters. Guo [30] proposed using a combination of quasi-static compression tests and machining tests to directly calculate the J-C parameters with the help of the Oxley model in 2003. Manes et al. [31] proposed using ballistic impact tests to achieve very high strain rate and instantaneous temperatures increase in the deformation zone for Al 6061-T6 in 2011. Starting in 2005, the popularity of finite element (FE) simulations in determining J-C parameters increased drastically, most likely because of the advancement in computers and computational technologies that made them cheaper and more accessible. One of early works in this context was published by Dabboussi and Nemes [32] who proposed using dynamic punch tests along with FE to iteratively search for J-C parameters. Shrot and Baeker [33] utilized finite element simulations, along with Levenberg-Marquardt search algorithm and orthogonal cutting tests to determine J-C parameters. Since then, many researchers have utilized orthogonal cutting tests and finite element simulations to determine J-C parameters, with different searching algorithms. Along with the use of FE simulations, the popularity of the Oxley model in simulating machining processes to determine J-C parameters was also remarkably high, as shown in Table 1.1. Among these works, Pang and Kishawy [34] used a novel inverse analysis to extract J-C parameters from orthogonal machining forces, avoiding the computationally heavy task of incrementally searching for the unknown Oxley variables including shear angle $\phi_c$, primary shear zone thickness ratio $C_0$, and secondary shear zone (tool-chip interface) thickness ratio $\delta$.

The overwhelming majority of the aforementioned research was based on the orthogonal turning method which is a simplified representation of cutting processes. Therefore, none of them could be directly applied to tools with complex geometry since majority of machining processes are in fact oblique processes. In oblique machining processes like milling, the chip thickness encountered by each tooth is variable during one revolution. In addition, the tool-workpiece engagement is varying along the tool axis due to the lag between consecutive teeth introduced by the helix angle. In addition, traditional methods of obtaining J-C parameters based on orthogonal machining require custom tool and experimental setup even for calibrating the force model for oblique machining processes. This step can be eliminated if a model capable of extracting the J-C parameters directly from oblique machining is available. A recent attempt to achieve this goal was made by Seif et al. [35], who extracted J-C parameters from the measured thrust force and torque of a drilling operation. They showed that the newly extracted J-C parameters could also be used in FE simulations to accurately predict cutting force, stress, strain, and temperature. Table 1.1 summarizes some of the research works aiming at extracting J-C parameters from machining data in chronological order.

Table 1.1: Summary of some important research in determining J-C parameters using different approaches.

| Year | Authors | Search Methods | Calculation Methods | Experiment Methods |
|---|---|---|---|---|
| 1997 | Rule [29] | Gradient based optimizer | Numerical integration of one-dimension model of Taylor specimen to obtain final specimen length, final undeformed length, and mushroom diameter. | Taylor impact tests |
| 2003 | Guo [30] | Linear regression | Using Oxley model to calculate shear strain rate | Quasi-static compression tests and machining tests |
| 2005 | Dabboussi and Nemes [32] | Iterative search | Finite element simulations to get force and displacement | Dynamic punch tests |
| 2007 | Ozel and Karpat [36] | Cooperative particle swarm optimization | Inverse Oxley model to get flow stress from machining measurements | Orthogonal cutting tests (turning) |
| 2011 | Manes et al. [31] | Optimization done using LS-OPT software | Finite element simulations | Ballistic impact tests |
| 2012 | Shrot and Baeker [33] | Levenberg-Marquardt search algorithm | Finite element simulations | Orthogonal cutting tests (turning) |

| | | | | |
|---|---|---|---|---|
| 2012 | Pang and Kishawy [34] | Genetic algorithm | Inverse Oxley model to get flow stress from machining measurements | Orthogonal cutting tests (turning) |
| 2013 | Klocke et al. [37] | Overshoot values and undershoot values then interpolate | Finite element simulations | Orthogonal cutting tests (turning) |
| 2013 | Bosetti et al. [38] | Nelder–Mead method and Nelder–Mead method and GA hybrid | Finite element simulations (Deform 2D) | Orthogonal cutting tests (turning) |
| 2016 | Franchi et al. [39] | Multi Island GA | Finite element simulations | Orthogonal cutting tests (turning) |
| 2018 | Ning et al. [40, 41] | Iterative gradient search method using Kalman filter algorithm | Forward Oxley model to calculate forces | Orthogonal cutting tests (turning) |
| 2019 | Seif et al. [35] | Nonlinear least-squares optimization | Forward Oxley model to calculate torque and force | Drilling pre-cored holes |
| 2021 | Hardt et al. [42] | Downhill-Simplex-Algorithm | Finite element simulations | Orthogonal cutting tests (turning) |
| 2021 | Eisseler et al. [43] | Iterative search | Finite element simulations (Deform 3D) | Orthogonal cutting tests (shaping machining) |

The work in this thesis goes beyond the simple machining methods to show that much more complex machining operations can also be implemented to obtain J-C parameters. The proposed model in this thesis is based on the Oxley model, which requires only workpiece material properties and cutting conditions as input variables to predict cutting forces, strain, strain rate, temperature, etc. [44]. Combining the J-C flow stress model with the Oxley machining model allows for the calculation of cutting forces for a wide range of cutting speed and feed. Utilizing this combined model with modern programming tools and optimization techniques allows for cutting force to be calculated for any arbitrarily complex tool geometries, specifically by dividing the complex cutting edges into many small segments then evaluate and summing cutting forces of all segments. The optimization techniques that are utilized in this thesis are Genetic Algorithm (GA), developed by Holland [45], and Particle Swarm Optimization (PSO), developed by Eberhart and Kennedy [46]. Both GA and PSO are metaheuristics optimization methods that are capable of randomly searching for a large solution space to find any unknown global optimum. GA involves a large population, encoding variables using binary strings to act as chromosomes, then use selection, crossover, and mutation operations to find the best variables' combination through a process that mimics natural selection, where the "fittest" chromosomes propagate to the next generations. The selection, crossover, and mutation procedures are conducted repeatedly on the population until a chromosome that satisfy fitness requirements is found. Similar to GA, PSO also involves a large population of particles, mimicking the behavior of a flock of birds or school of fish to search for a best solution in a large solution space. This thesis analyzes and compares GA and PSO in terms of the quality of solutions as well as the rate of converging toward the optimum solution. GA and PSO were initially used in finding a combination of J-C parameters that yields the best agreement between the calculated and measured (experiment) cutting forces. GA and PSO were then implemented in solving the unknown Oxley variables, namely primary shear zone thickness ratio ($C_0$), secondary shear zone (tool-chip interface) thickness ratio ($\delta$), and shear angle ($\phi_c$) as opposed to using incremental search. Strain rate hardening and thermal softening effects are accounted for within the Oxley model, thus the method presented drastically reduces testing complexity by eliminating the need for directly measuring temperature and deformation rate at the shear zones.

## 1.3 Research Objective

The main objective of this thesis is to propose a forward determination method for estimating J-C parameters from any arbitrary complex machining operations, and to apply this model to both regular wrought metals and AM metals. Specifically, the research in this thesis aims to:

- Develop a cutting force prediction model for complex cutter geometry, specifically end milling.
- Apply optimization algorithms to solve Oxley variables and search J-C dynamic parameters from end milling.
- Apply the proposed method to obtain J-C dynamic parameters for regular wrought metals and compare the results with those obtained using existing methods.
- Apply the proposed method to obtain J-C dynamic parameters for AM titanium Ti-6Al-4V and compare the results with regular wrought titanium.
- Investigate the potential variation of cutting forces, J-C parameters, and chip morphology during the machining of AM titanium Ti-6Al-4V in different directions versus printing direction, as well as versus wrought titanium.

# Chapter 2

# Machining and Optimization Models

## 2.1 Preamble

The field of machining has been greatly influenced by the Oxley machining model, which is widely used to simulate the process of chip formation and cutting forces. However, this model relies on a simplifying assumption that the shear zone is a two-dimensional (2D) plane, which might not be representative of the actual machining process. This thesis utilizes a more realistic assumption by using the extended thick shear zone model developed by Pang and Kishawy [34] and then further extended again by Pang et al. [47].

Firstly, this chapter presented a detailed calculation procedure of this extended thick shear zone model, with the aim of providing a clear and accessible framework for ease of replication. As such, this chapter provides formulas and methodology for calculating every variable required. Additionally, figures are included to visualize the balance of forces acting on the tool rake face and shear plane. Finally, the conditions for solving the three unknown variables are also explained in detail.

Secondly, this chapter explained the method of dividing the end mills into many small elements, which demonstrated how cutting forces for complex tool geometry can be calculated, such as end milling.

Thirdly, two metaheuristic algorithms, GA and PSO are used and compared. Each will be used to calculate the cutting forces generated from each element, and then used once again to search for a combination of J-C parameters such that the net predicted cutting forces matches the net measured cutting forces. This chapter explained the double usage of each optimization algorithm as the inner layer search (Oxley search) and the outer layer search (J-C search).

Finally, this chapter includes the explanation of four major types of chip formation, discontinuous chips, continuous chips, continuous chips with built-up edge (BUE), and serrated chips. Each type is characterized by its own features and factors that contribute to its formation. This chapter provides a brief overview of each type, including the materials in which they are commonly observed, the factors that contribute to their formation, and the impact they have on the final surface quality. This serves as context for the observed chips presented in the results and discussion chapter.

## 2.2 Oxley Machining Model

Over the years, many researchers have expanded on the Oxley machining model to give more realistic assumptions of the shear zone. To make it easier to follow the approach and to duplicate the work, the underlaying formulas for this model is presented in detail. The particular extended thick shear zone model utilized in this thesis is the one developed by Pang and Kishawy [34], whereby the shear zone as a thick region contained by two parallel sides. These two sides have unequal distance from the

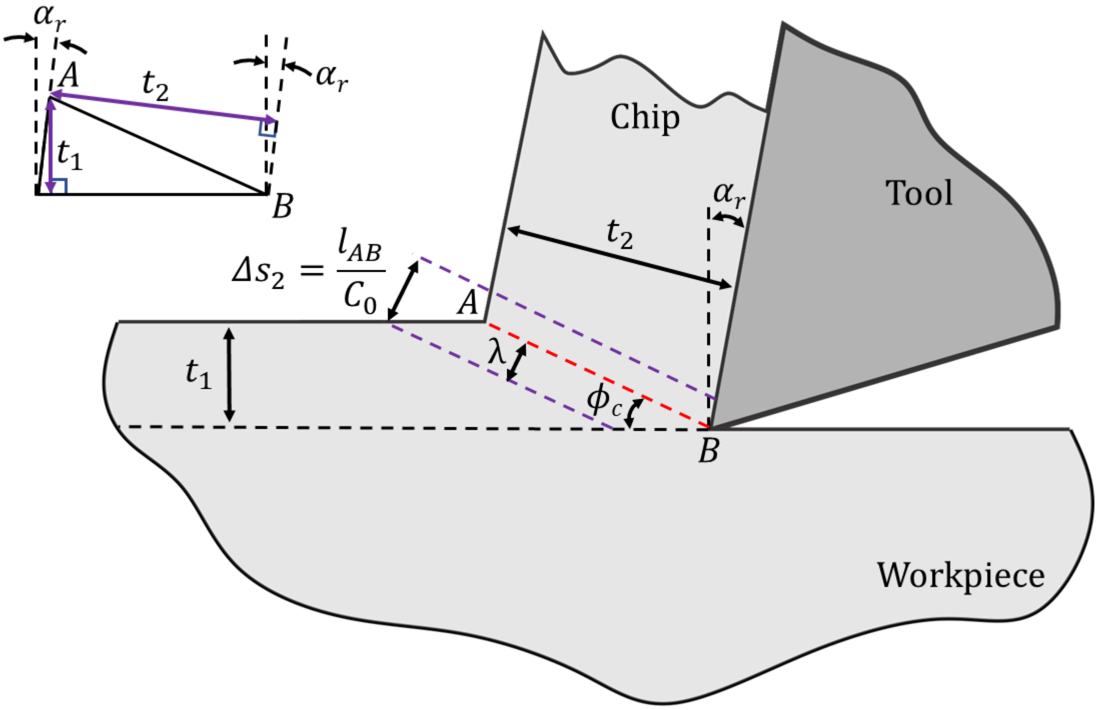

Figure 2.1: Un-equidistant thick parallel shear zone.

primary shear zone AB, see Fig. 2.1. The lower region has a thickness of $\lambda$. The shear line AB extends from the tip of the cutting edge up to the free surface where the chip starts. The transition between workpiece surface to chip is simplified to be instantaneous, thus point A is located at the sharp corner. The length of shear line AB can then be calculated as a function of undeformed chip thickness $t_1$ and shear angle $\phi_c$, see Eq. 2.1.

$$l_{AB} = \frac{t_1}{\sin \phi_c} \tag{2.1}$$

The deformed chip is simplified to have a constant thickness from the moment it is formed to when it loses contact with the rake face. The deformed chip thickness is measured from the free surface down perpendicular to the rake face, see Fig. 2.2. Eq. 2.2 shows the geometric relationship between undeformed chip thickness $t_1$ and deformed chip thickness $t_2$.

$$t_2 = t_1 \frac{\cos(\phi_c - \alpha_r)}{\sin \phi_c} \tag{2.2}$$

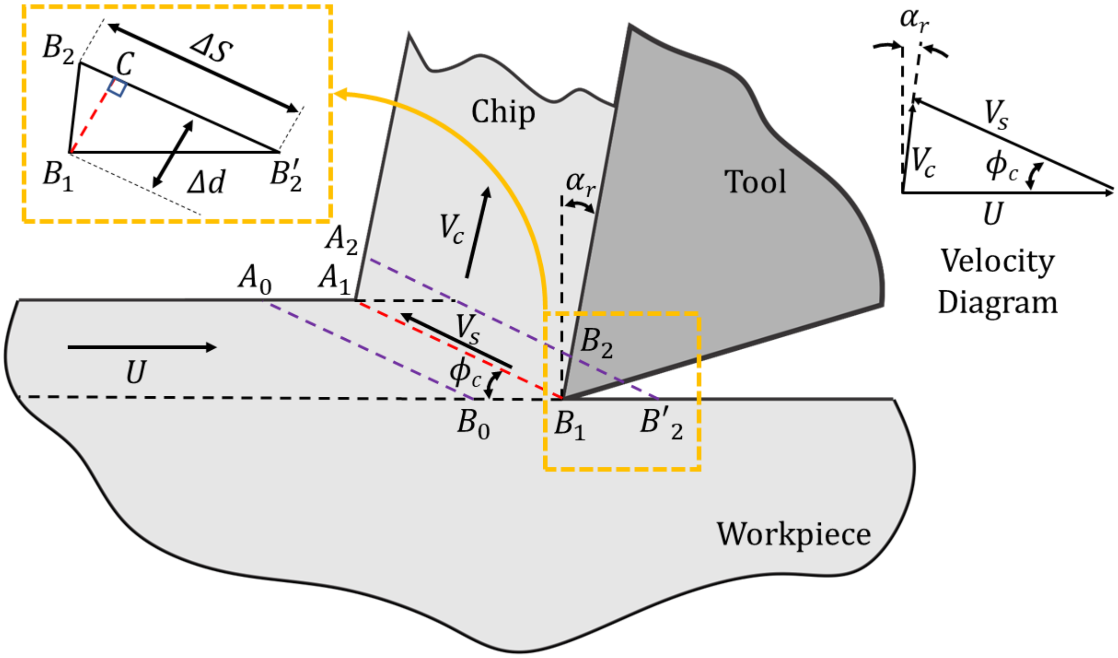

Figure 2.2: Geometric relationship between shear deformation, shear angle and rake angle.

Shear strain from chip formation can be simplified using Piispanen Model of Card Analogy. An element begins as the parallelogram $A_0A_1B_1B_0$. As the tool moves forward and come into contact with the element, it deforms from the shape of $A_1A_2'B_2'B_1$ to the shape of $A_1A_2B_2B_1$, as shown in Fig. 3. Thus, shear deformation can be visualized as the movements of material with distance of $\Delta S$. The element has a thickness of $\Delta d$, therefore, by definition, the shear strain $(\gamma_{AB})$ along shear plane is the shear distance $\Delta S$ divided by element thickness $\Delta d$, as shown in Eq. 2.3.

$$\gamma_{AB} = \frac{\Delta \mathrm{S}}{\Delta \mathrm{d}} = \frac{B_2'C}{B_1C} + \frac{B_2C}{B_1C} = \cot\phi_c + \tan(\phi_c - \alpha_r) \tag{2.3}$$

Based on von Misses yield criterion; the equivalent shear strain $(\epsilon_{AB})$ can be calculated from shear $\gamma_{AB}$ using Eq. 2.4 [48].

$$\epsilon_{AB} = \frac{\gamma_{AB}}{\sqrt{3}} = \frac{1}{2\sqrt{3}} \cdot \frac{\cos\alpha_r}{\cos(\phi_c - \alpha_r)\sin\phi_c} \tag{2.4}$$

Shear velocity ($V_S$) is parallel to shear plane and chip velocity ($V_C$) is parallel to rake face. The relationship between $V_S$ and cutting velocity ($U$) is presented in Eq. 2.5.

$$V_S = U \frac{\cos \alpha_r}{\cos(\phi_c - \alpha_r)} \tag{2.5}$$

Strain rate can be obtained by examining the shear zone. The parallel shear zone model assumes the shear zone can be defined between two parallel lines with the shear zone thickness $\Delta s_2$ [34], as shown in Fig. 2.2. Based on von Misses yield criterion; the equivalent shear strain rate ($\dot{\epsilon_{AB}}$) can be calculated from shear strain rate ($\dot{\gamma_{AB}}$) along shear plane [48], see Eqs. 2.6 and 2.7.

$$\dot{\gamma_{AB}} = \frac{V_S}{\Delta s_2} = V_S \frac{C_0}{l_{AB}} \tag{2.6}$$

$$\dot{\epsilon_{AB}} = \frac{\dot{\gamma_{AB}}}{\sqrt{3}} = \frac{1}{\sqrt{3}} V_S \frac{C_0}{l_{AB}} \tag{2.7}$$

By analyzing the velocity boundary conditions and changes in the shear strain rate when material enters and exit the shear zone, the relationship between lower region thickness ratio ($\lambda$) with $\phi_c$ and $\alpha_r$ can be established [34].

$$\lambda = \frac{\cos \phi_c \cos(\phi_c - \alpha_r)}{\cos \alpha_r} \tag{2.8}$$

$$n_{eq} = \frac{nB\epsilon_{AB}^n}{A + B\epsilon_{AB}^n} \tag{2.9}$$

$$\theta = \arctan\left[1 + 2\left(\frac{\pi}{4} - \phi_c\right) - \frac{C_0}{\lambda} n_{eq}\right] \tag{2.10}$$

$$R_T = \frac{\rho S U t_1}{K} \tag{2.11}$$

$$\text{If } 0.04 \leq \ R_T tan\phi_c \leq 10 \rightarrow \beta = 0.5 - 0.35 \times \log(R_T tan\phi_c) \tag{2.12}$$

$$\text{If } 10 \leq \ R_T tan\phi_c \rightarrow \beta = 0.3 - 0.15 \times \log(R_T tan\phi_c) \tag{2.13}$$

The primary shear zone temperature, shear force, and shear stress are directly connected to one another. As shearing action occurs, heat is generated and cause temperature to increase. As temperature increases, shear flow stress decreases, thus reducing shear force. Reduced shear force generates less heat. Therefore, these three variables will take values such that they are in equilibrium. The incremental search is conducted to find the appropriate shear zone temperature ($T_{AB}$) that satisfies all three equations. Based on von Misses yield criterion; the equivalent shear flow stress ($k_{AB}$) can be calculated from the shear stress ($\sigma_{AB}$) along shear plane [48].

$$k_{AB} = \frac{\sigma_{AB}}{\sqrt{3}} = \frac{1}{\sqrt{3}}\left(A + B\epsilon_{AB}^{n}\right)\left[1 + C\ln\left(\frac{\dot{\epsilon_{AB}}}{\dot{\epsilon_0}}\right)\right]\left[1 - \left(\frac{T_{AB} - T_0}{T_m - T_0}\right)^{m}\right] \tag{2.14}$$

Shear force ($F_S$) is calculated from $k_{AB}$, $l_{AB}$, and the width of cut ($w$).

$$F_S = k_{AB} l_{AB} w \tag{2.15}$$

The temperature at the shear zone is elevated from ambient workpiece temperature due to the shearing action.

$$T_{AB} = T_w + \eta\frac{1-\beta}{\rho S t_1 w} \times \frac{F_S \cos\alpha_r}{\cos\left(\phi_c - \alpha_r\right)} \tag{2.16}$$

Assuming that the tool moves at a constant speed, the normal force and friction force experienced by the tool rake face has to be in equilibrium with the shear force and normal force on the shear plane. Merchant's circle is a great tool to visualize this balance of forces, as shown in Fig. 2.3, and it is used to derive Eqs. 2.17 to 2.20.

$$F_F = F_S\frac{\sin\left(\theta - \phi_c + \alpha_r\right)}{\cos\theta} \tag{2.17}$$

$$F_{NF} = F_S\frac{\cos\left(\theta - \phi_c + \alpha_r\right)}{\cos\theta} \tag{2.18}$$

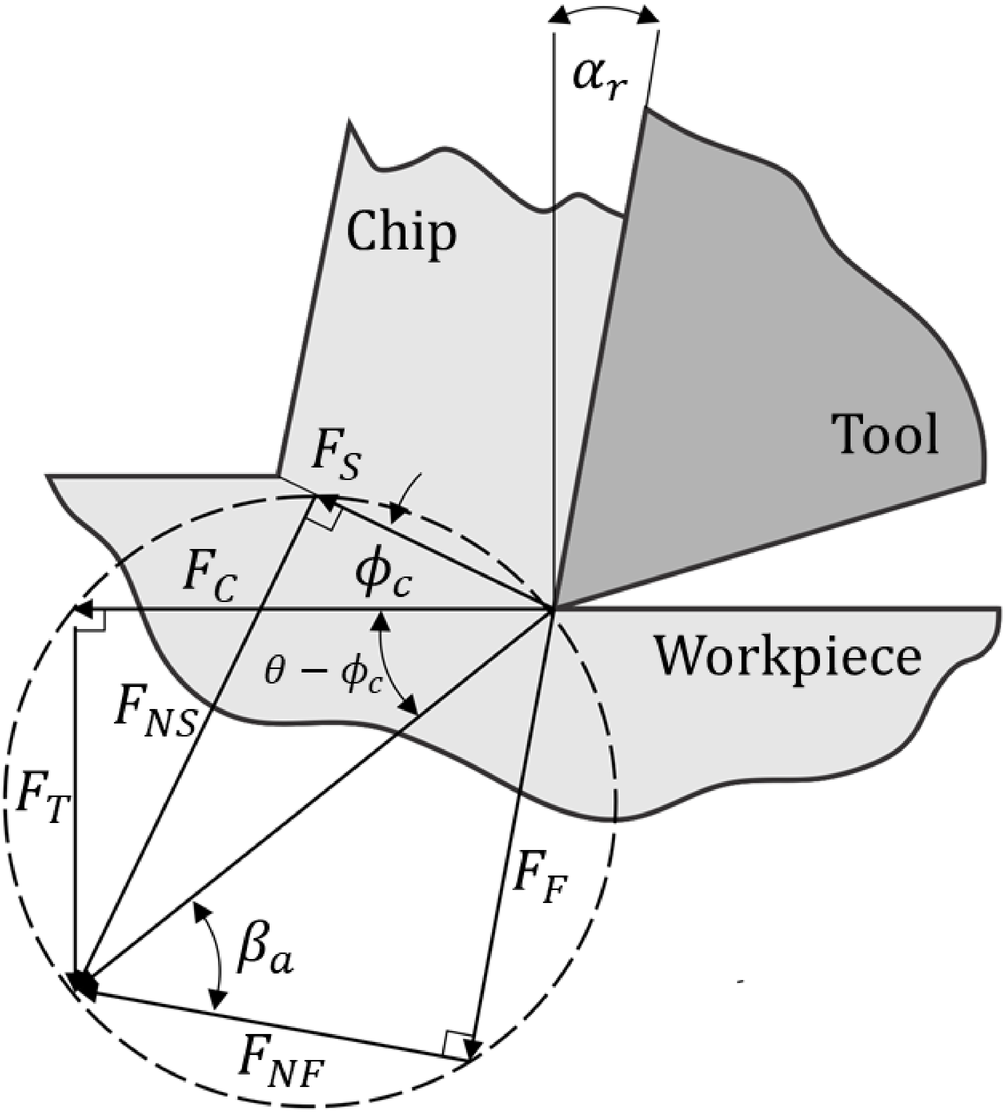

Figure 2.3: Forces balance using Merchant's circle.

$$F_C = F_S \frac{\cos(\theta - \phi_c)}{\cos\theta} \tag{2.19}$$

$$F_T = F_S \frac{\sin(\theta - \phi_c)}{\cos\theta} \tag{2.20}$$

The net resultant force acting on the shear plane is balanced with the resultant force acting on the rake face of the cutting tool, as shown in Fig. 2.4. The hydrostatic stress at point A and B on the shear plane AB can be solved based on Eq. 2.21 and 2.22 respectively. The distance between the cutting edge to the net resultant force on shear

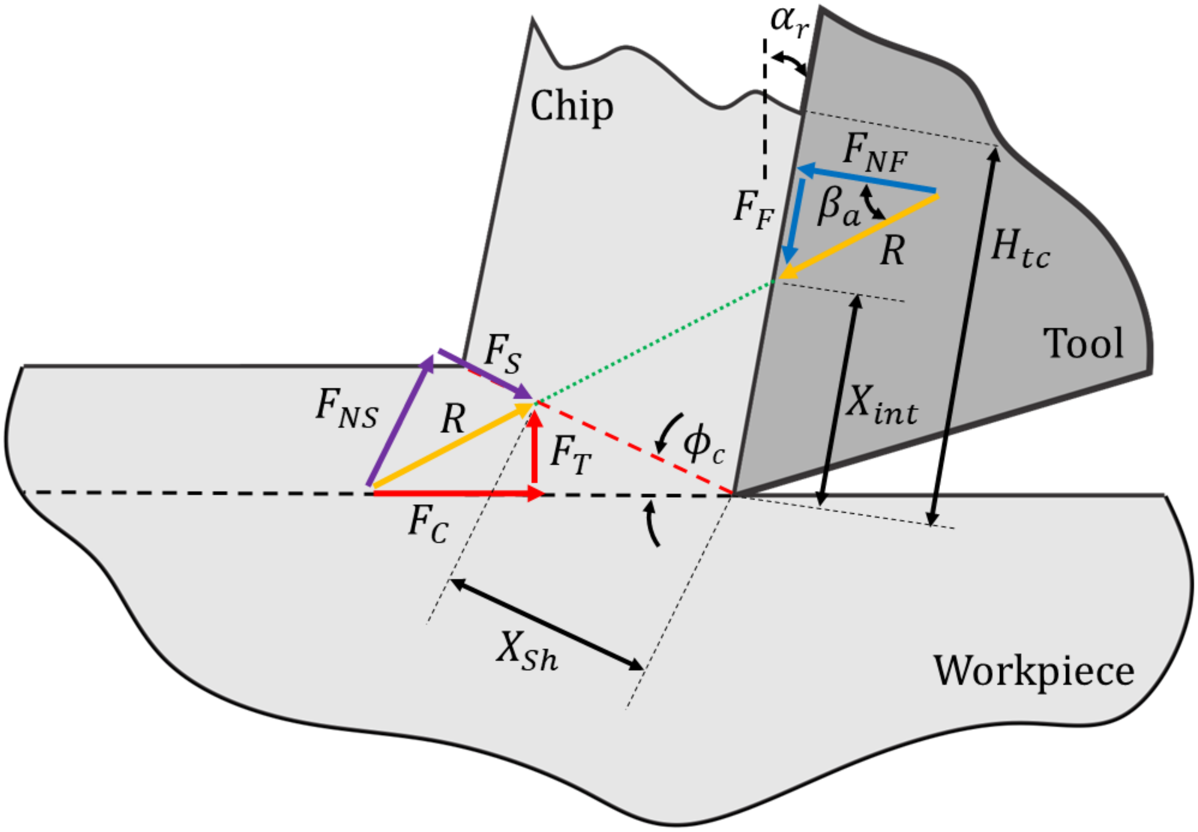

Figure 2.4: Forces balance and net force locations.

plane and the rake face can be solved based on Eq. 2.23 and 2.24 respectively. [47]

$$P_A = k_{AB}\left[1 + 2\left(\frac{\pi}{4} - \phi_c\right)\right] \tag{2.21}$$

$$P_B = P_A - 2k_{AB}\frac{C_0}{\lambda}n_{eq} \tag{2.22}$$

$$X_{sh} = \frac{2P_A + P_B}{3\left(P_A + P_B\right)}l_{AB} \tag{2.23}$$

$$X_{int} = X_{sh}\frac{\sin\theta}{\cos\left(\theta - \phi_c + \alpha_r\right)} \tag{2.24}$$

Assuming that the net force acting on the tool rake face is in the middle of the tool-chip interface length, then the total tool-chip contact length ($H_{tc}$) is twice of the location of the resultant force acting on the tool-chip interface ($X_{int}$), as shown in Eq. 2.25. Strain, strain rate, and temperature at the secondary shear zone (tool-chip interface) can be solved based on Eqs. 2.26 to 2.29.

$$H_{tc} = 2X_{int} \tag{2.25}$$

$$\epsilon_{int} = \frac{1}{\sqrt{3}} \cdot \frac{H_{tc}}{\delta t_2} \tag{2.26}$$

$$\dot{\epsilon_{int}} = \frac{1}{\sqrt{3}} \cdot \frac{V_C}{\delta t_2} = \frac{1}{\sqrt{3}} \cdot \frac{U \sin \phi_c}{\cos\left(\phi_c - \alpha_r\right)} \cdot \frac{1}{\delta t_2} \tag{2.27}$$

$$\Delta T_C = \frac{F_F \sin \phi_c}{\rho S t_1 w \cos\left(\phi_c - \alpha_r\right)} \tag{2.28}$$

$$T_{int} = T_{AB} + \psi \cdot \Delta T_C \cdot 10^{\left[0.06 - 0.195\delta\left(\frac{R_T t_2}{H_{tc}}\right)^{0.5} + 0.5 \log\left(\frac{R_T t_2}{H_{tc}}\right)\right]} \tag{2.29}$$

There are three variables in the Oxley model that cannot be calculated directly. These variables are the primary shear zone thickness ratio ($C_0$), secondary shear zone (tool-chip interface) thickness ratio $\delta$, and shear angle $\phi_c$. The optimization search based on GA is utilized in this thesis to find the solution to these variables. The solution is a combination of $C_0$, $\delta$, and $\phi_c$ such that three conditions are satisfied simultaneously. The first condition to satisfy requires that the two methods of calculating normal stress on tool-chip interface agree such that $\sigma_N = \sigma'_N$. The first method calculates normal stress ($\sigma_N$) from hydrostatic pressure at point $B$. The second method calculates normal stress ($\sigma'_N$) from normal force and tool-chip interface area.

$$\sigma_N = P_B + 2k_{AB}\left(\phi - \alpha\right) \tag{2.30}$$

$$\sigma'_N = \frac{F_N}{H_{tc} w} \tag{2.31}$$

The second condition to satisfy entails that the two methods of calculating shear stress on tool-chip interface matches, such that $\tau_{int} = \tau'_{int}$. The first method calculates the shear flow stress ($\tau_{int}$) on the tool-chip interface using J-C constitutive formula. The second method calculates the same shear flow stress ($\tau'_{int}$) from the friction force and tool-chip interface area.

$$\tau_{int} = \frac{1}{\sqrt{3}} \left(A + B\epsilon_{int}^{n}\right) \left[1 + C \ln\left(\frac{\dot{\epsilon_{int}}}{\dot{\epsilon_0}}\right)\right] \left[1 - \left(\frac{T_{int} - T_0}{T_m - T_0}\right)^{m}\right] \tag{2.32}$$

$$\tau'_{int} = \frac{F_F}{H_{tc} w} \tag{2.33}$$

The last condition enforces the combination of variables $C_0$, $\delta$, and $\phi_c$ to minimize the cutting force ($F_C$).

## 2.3 Complex Profile Cutting Tools Model

As mentioned earlier, the majority of previously developed models for determining the J-C parameters rely on orthogonal testing. It means even for simulating cutting forces in machining processes where the nature of tool-workpiece engagement is oblique, performing orthogonal testing is still inevitable. In this section, the previously described Oxley thick shear zone model is applied directly to milling where geometry of tool-workpiece engagement is complex. A milling tool has multiple cutting edges that enter and exit the cut periodically. This interrupted cutting leads to the unavoidable mechanical and thermal shocking. To reduce the intensity of this issue, end mills typically have helical teeth that gradually enter and exit the workpiece material. The helical geometry distributes the cutting forces more evenly thus reduces maximum cutting forces while maintaining the exact same material removal rate. Calculating cutting forces for helical end mills requires sectioning the cutting edges into disk elements, as shown in Fig. 2.5.

Cutting force magnitude and direction for each element inside the cut region is calculated and integrated along the cutting edge. The resultant milling forces acting on the tool are the summations of all elemental forces acting on each tooth. Depending on the current tool rotation angle, the engagement angle of the element at the bottom

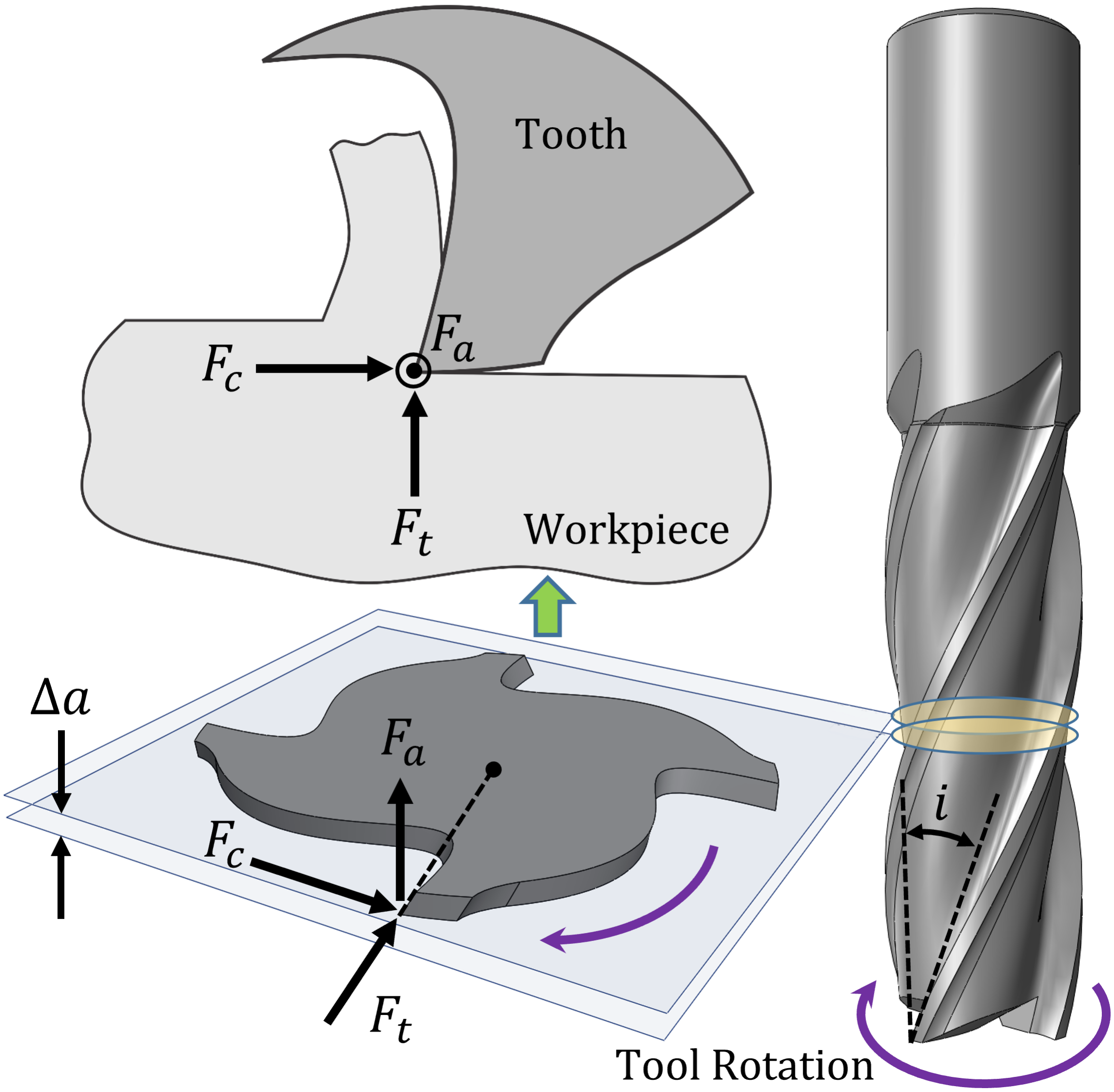

Figure 2.5: Dividing end mill into segments.

of the tool is defined by $\phi_{flute}$. Since the tooth is helical, the engagement angle for any element at height $z_{height}$ lags behind the very bottom element, which be defined as:

$$\phi_{segment} = \phi_{flute} - \frac{2}{D} \cdot \tan\left(i_{helix}\right) \times z_{height} \tag{2.34}$$

If $\phi_{st} < \phi_{element} < \phi_{ex}$, then the element is engaged with the workpiece, thus cutting forces are present; otherwise, that element is not in cut and therefore does not contribute to the cutting forces at that moment. The instantaneous uncut chip thickness

$t_1$ of this segment depends on the element engagement angle $\phi_{element}$.

$$t_1 = s_t \sin\left(\phi_{element}\right) \tag{2.35}$$

The tool helix angle is the inclination angle in oblique cutting. As a result, an axial component of force parallel to the end mill is generated. Due to the inclined rake face, the chip flows on the rake face with additional angles namely, normal shear angle ($\phi_n$), normal friction angle ($\beta_n$), and chip flow angle ($\eta_c$). The normal shear angle is approximately equal to the shear angle that occurs in orthogonal cutting ($\phi_n = \phi_c$). Similarly, for normal rake angle ($\alpha_n = \alpha_r$). The normal friction angle and chip flow angles take values such that they are the solution to the system of equations Eq. 2.36 and Eq. 2.37 [49]. These equations are non-linear, therefore, solving the unknown variables are done by isolating each one of them, then applying Newton's method to find the roots.

$$\tan\beta_n = \tan\beta\cos\eta_c \tag{2.36}$$

$$\tan\left(\phi_n + \beta_n\right) = \frac{\cos\alpha_n \tan i}{\tan\eta_c - \sin\alpha_n \tan i} \tag{2.37}$$

The axial force is then calculated as a function of cutting force, thrust force, helix angle, rake angle, and chip flow angle as shown.

$$F_a = \frac{F_c\left(\sin i - \cos i \sin\alpha_n \tan\eta_c\right) - F_t \cos\alpha_n \tan\eta_c}{\sin i \sin\alpha_n \tan\eta_c + \cos i} \tag{2.38}$$

Width of cut ($w$) of the segment depends on how small the cutting edge is divided into ($w = \Delta a$). Cutting forces contribution of each segment is then separated into their x, y, and z-components, then summed to obtain the total cutting forces.

$$F_x = \sum_{i=1}^{N}\left[F_c\left(i\right)\cos\phi\left(i\right) + F_t\left(i\right)\sin\phi\left(i\right)\right] \tag{2.39}$$

$$F_y = \sum_{i=1}^{N} \left[ F_c(i) \sin\phi(i) - F_t(i) \cos\phi(i) \right] \tag{2.40}$$

$$F_z = \sum_{i=1}^{N} \left[ F_a(i) \right] \tag{2.41}$$

## 2.4 Population-Based Optimization

### 2.4.1 Genetic algorithm

First developed by John Holland [45], GAs are evolutionary algorithms used to find optimal solutions to problems by mimicking the natural selection process. GA involves manipulating a population of chromosomes, whereby each chromosome encodes the variable values of the problem to be solved. Just like in nature, each chromosome went through fitness evaluations, crossover, and mutation. Chromosomes that return better results in an optimization problem will have a higher chance of crossover to create offspring, and therefore, pass on its desirable characteristics to the next generations. This natural process happens over many generations until an acceptable optimization result is found.

Chromosome encoding allows for the manipulation of multiple variables at once. Encoding converts a series of variables into a single binary string. Thus, each segment of the string represents a variable, as shown in Fig. 2.6. Higher number of binary bits results in higher search resolution. Typically, the total number of binary bits in a chromosome is distributed evenly among all variables. The binary strings represent the location of the variable in between the allowable minimum value ($x_{min}$) and the maximum value ($x_{max}$). A binary string of zeroes (0s) represents the smallest variable value, and a binary string of ones (1s) represents the largest variable value. Decoding binary string to value is done by first converting the binary string in base 2 to base 10, as shown in Eq. 2.42. Then, this base 10 number is the position of the variable in

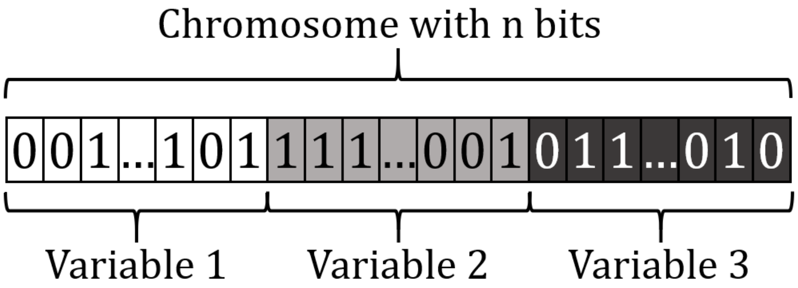

Figure 2.6: Binary string of an encoded individual.

between the $x_{min}$ and $x_{max}$. The search resolution is given by dividing the difference between $x_{min}$ and $x_{max}$ with $2^{n-1}$, where n is the number of binary bits.

$$\text{Position} = \sum_{i=0}^{n-1} \left(b_i \times 2^i\right) \tag{2.42}$$

$$x = x_{min} + \frac{\text{Position}}{2^n - 1}\left(x_{max} - x_{min}\right) \tag{2.43}$$

In this thesis, there are two optimization problems to be solved, with one optimization nested inside the other. The first optimization problem searches for the unknown variables $C_0$, $\delta$, and $\phi_c$ needed in the Oxley model such that all three search conditions (see the end of section 2.2) are satisfied, as shown in Eq. 2.44. The first optimization is done for every cutting edge element; thus, it is nested within the cutting force integration loop of the second optimization problem. The second optimization problem searches for the set of J-C parameters that minimizes the difference between calculated cutting force and measured cutting force, as shown in Eq. 2.45.

$$(C_0,\ \delta,\ \phi_c) = min\left\{\left|1 - \frac{k_{int}}{\tau_{int}}\right| + \left|1 - \frac{\sigma'_N}{\sigma_N}\right| + F_C\right\} \tag{2.44}$$

$$(A,\ B,\ C,\ n,\ m) = min\left\{\left|1 - \frac{F_{measured}}{F_{calculated}}\right|\right\} \tag{2.45}$$

The fitness evaluation scores the individuals in the population. Individual with a higher fitness score has a higher probability of being chosen as one of the crossover parents. In this thesis, the fitness proportionate selection (roulette wheel selection) is utilized, whereby the selection probability is calculated based on Eq. 2.46.

$$p_i = \frac{k_i}{\sum_{j=1}^{N} k_j} \tag{2.46}$$

Because objectives are both minimization problems, the fitness value of each individual ($k_i$) is calculated by taking the highest objective function value of the population ($f_{max}$) and subtracting the objective function value of that individual ($f_i$), as shown in Eq. 2.47.

$$k_i = f_{max} - f_i \tag{2.47}$$

Crossover is a process that involves two or more chromosomes. These chosen chromosomes are called parents. Offspring is created by recombining the binary strings of the parents in a random manner. The binary segments between the cut points are swapped between the parents, the resulting offspring are new chromosomes, as shown in Fig. 2.7. For two-point crossover, to reduce the likelihood that the crossover operation creates clones of the parents, the distance between the two cut locations (cut length) is set to a typical minimum of 5 bits. Accidental cloning happens when the swapping segments are identical, which is more likely to happen when the cut length is small.

The mutation operation is applied immediately after crossover. Mutation works by flipping the binary bits of chromosomes, from 0 to 1, or from 1 to 0, as shown in Fig. 2.7. The crossover operation allows the population to converge to an optimal location in the search space, while the mutation operation introduces chaos and thereby encourages exploration of the search space.

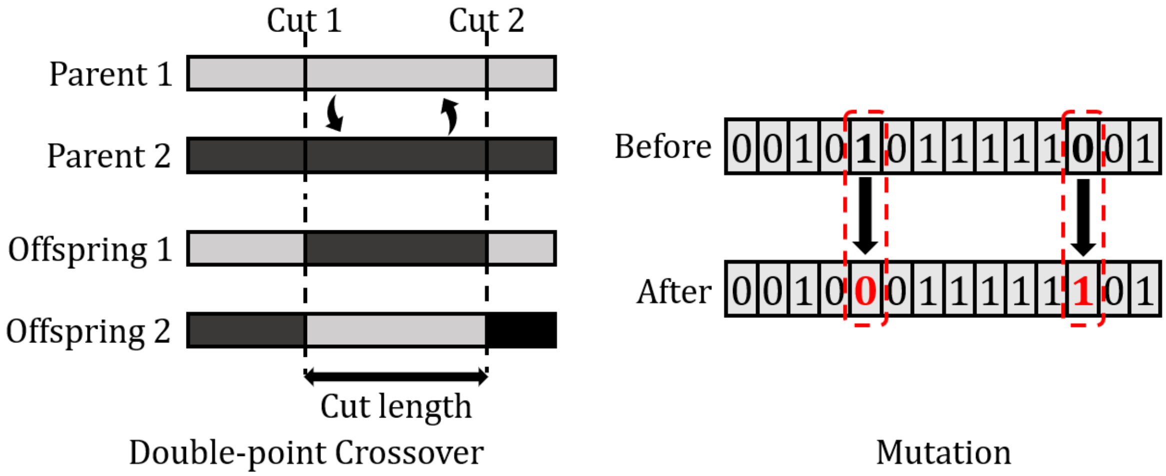

Figure 2.7: Crossover operation and mutation operation.

### 2.4.2 Particle swarm optimizer

First developed by Eberhart and Kennedy [46], PSO is a population-based meta-heuristic algorithm. Analogous to the behavior of a school of fish or a flock of birds, each particle moves around within the solution space through iterations. Particles move based on two parameters, $C_1$ which is the cognitive learning factor, and $C_2$ which is the social learning factor. The cognitive learning factor gives particles a tendency to move around their own personal best solution, $p_i$, while the social learning factor gives particles a tendency to move closer to the current best solution in the entire population, $p_g$. Randomness is introduced using coefficients $\rho_1$ and $\rho_2$, which are generated between 0 and 1 for every velocity calculation. Velocity, which represents how fast a particle moves through the solution space in each iteration, is calculated according to Eq. 2.48.

$$v_i\left(t\right) = w \times \ v_i\left(t-1\right) + \rho_1 C_1 \times \left(p_i - x_i\left(t-1\right)\right) + \rho_2 C_2 \times \left(p_g - x_i\left(t-1\right)\right) \tag{2.48}$$

In addition, weighting factor ($w$) augments particles' velocities over time. Initially, the weighting factor is high to encourage exploration, then over time, the weighting factor decreases to encourage deeper local search. The objective function for PSO algorithm is the same as that of GA algorithm, presented in Eqs. 2.44 and 2.45.

## 2.5 Johnson-Cook Parameter Determination Model

The strain rate hardening coefficient $C$ and the thermal softening exponent $m$ are difficult to obtain, thus they are the focus of this algorithm, see Fig. 2.8 and Fig. 2.9. The algorithm starts by initializing the first randomized population containing different sets of $C$ and $m$.

These sets are then used in combination with other J-C parameters $A$, $B$, and $n$,

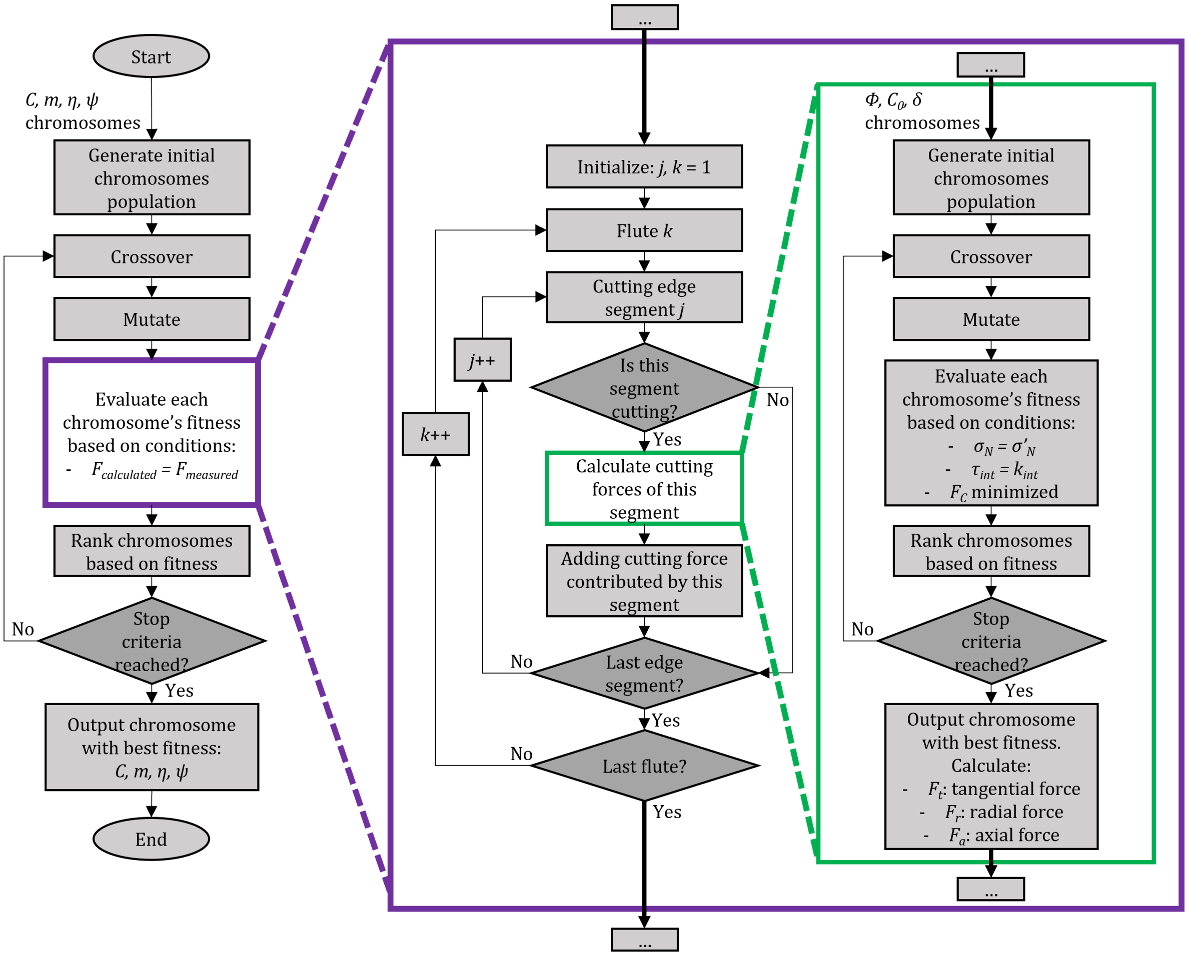

Figure 2.8: Block diagram procedure of search for J-C parameters using GA.

which are obtained from quasi-static tests to calculate the cutting forces utilizing the

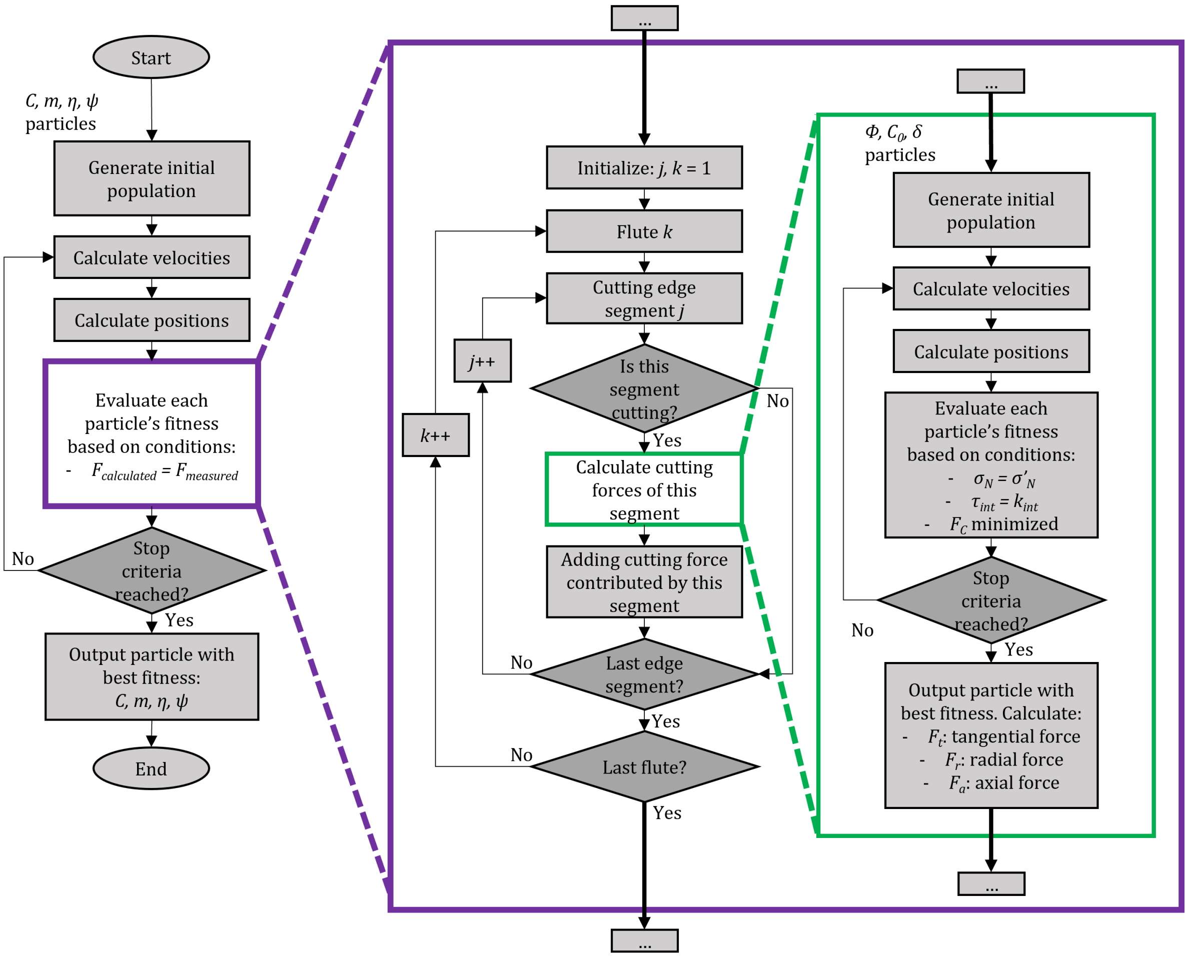

Figure 2.9: Block diagram procedure of search for J-C parameters using PSO.

Oxley model.

As discussed in section 2.3, cutting forces are calculated by dividing the end mill cutting edges into finite disk elements. The cutting force for each element is then evaluated and summed to obtain the total cutting forces. Force calculation is done until all elements for the entire tool are accounted for. Solving the cutting force of each element using Oxley model requires an additional nested GA search to solve the three variables $C_0$, $\delta$, and $\phi_c$. This GA also goes through the initial population generation, evaluation, crossover, and mutation until the objective function is sufficiently achieved, see Eq. 2.44. Returning to the main outer GA, the population then goes through crossover, mutation, looping until a set of J-C parameters that sufficiently satisfy Eq. 2.45 is found.

The block diagram procedure of PSO is similar to GA, as shown in Fig. 2.9. The difference between PSO and GA is how successive iterations are generated. The strategy for nested search of Oxley variables, and outer search of J-C parameters are the same for both GA and PSO, only their implementation is different. This is to show that any optimization scheme can be used, either GA or PSO, or any similar heuristic optimization algorithms.

## 2.6 Mechanics of Chip Formation

The mechanics of chip formation can be grouped into four major types according to Trent et al. [50]. These are discontinuous chip, continuous chip, continuous chip with built-up edge (BUE), and serrated chip, as shown in Fig. 2.10.

The first main type of chips is discontinuous chips. Discontinuous chips are characterized by small, individual pieces resulted from the fracture of the chips. Each fracture is formed when a crack initiates at the tool tip and propagates towards the free surface [21]. This occurs randomly, meaning the fractured pieces can vary in size, shape, and level of attachment to each other. This type of chip formation is commonly observed when machining brittle materials, as well as those containing hard inclusions or impurities, such as graphite flakes found in cast iron. Additionally, factors such as low or high cutting speeds, small rake angles of cutting tools, high friction at the tool-chip interface, and low stiffness of machine tools can contribute to the production of discontinuous chips. Although discontinuous chip formation often results in poor surface finish, it can be advantageous during heavy roughing operations, as these chips are easier to dispose of than longer continuous chips.

The second type of chips produced during metal machining is known as continuous chips. These types of chips flow continuously without breakage. They are likely to

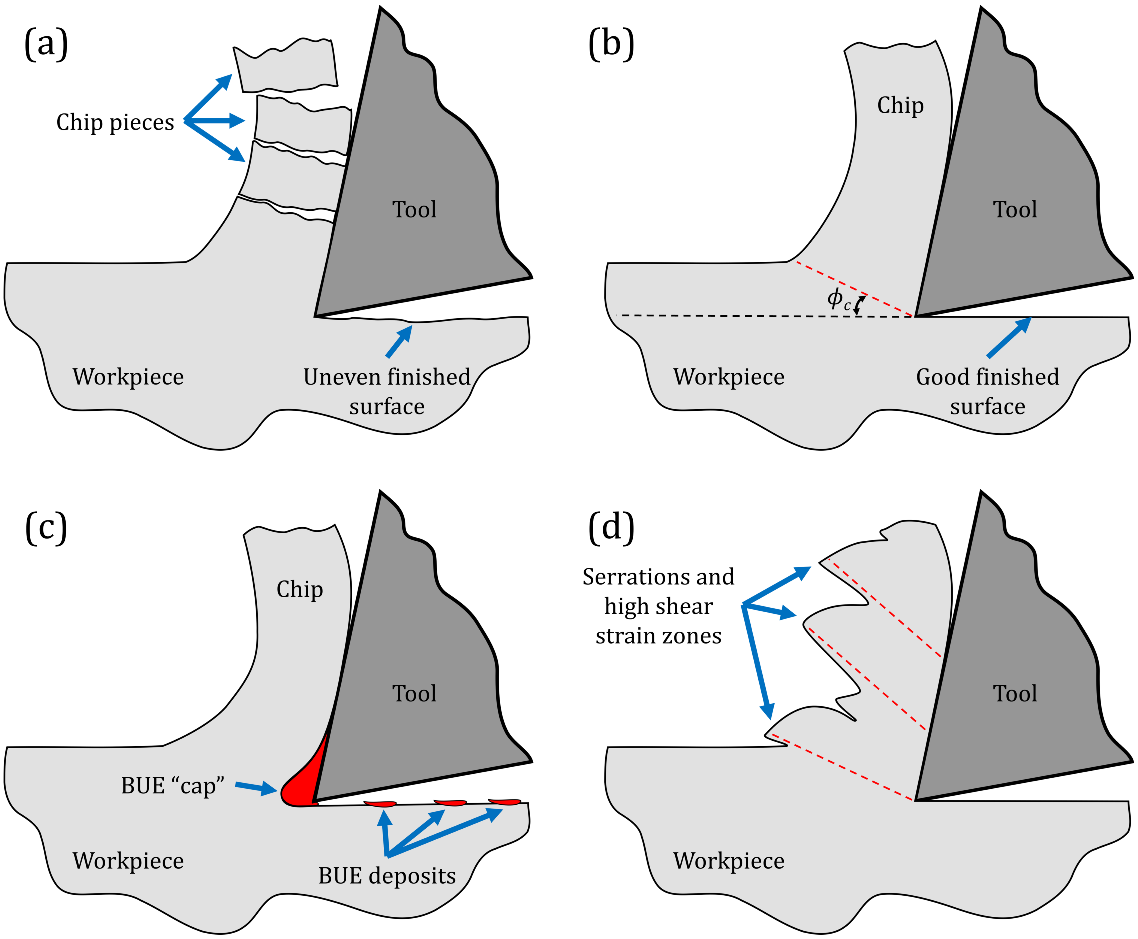

Figure 2.10: Four main types of chip formation, (a) discontinuous, (b) continuous, (c) continuous with BUE, and (d) serrated chips.

form when homogeneous metals are machined. The shearing action occurred is concentrated along a thin shear plane with no plastic deformation occurring before or after the shear zone [21]. Continuous chips are most likely to appear during high-speed machining of ductile materials with small feeds and depth of cut, using sharp cutting tools with low tool-chip friction and high rake angles. Although continuous chips typically result in a smooth surface finish, their length can pose a challenge for disposal and may cause machine or workpiece entanglement. To address this issue, some cutting tools are specifically designed to break long chips into smaller, more manageable lengths [51].

The third type of chips is continuous chip with BUE. This type of chips is very similar to the continuous chip, but with a caveat that material adheres to the cutting edge, creating a severely strain hardened “cap” [50]. This type of chip formation is most likely to occur when machining ductile materials at low-to-medium cutting speeds, especially when cutting with tools that have a blunt cutting edge and under dry machining conditions. The BUE temporarily protects the cutting edge from wear but can also lead to unstable cutting if it breaks off, which leaves scratches and BUE particles on the machined surface, negatively affects surface quality. The strain hardened BUE “cap” at the tip of the cutting tool also changes the geometry of the cutting edge and negatively impact surface quality by reducing its smoothness and uniformity.

The last type of chips is serrated chips, also known as saw-toothed chips. These are semi-continuous chips that exhibit zones of low and high shear strain resulting in a distinctive saw-tooth appearance. The formation of serrated chips is typically observed in materials that have high strain hardening behavior and low thermal conductivity, such as titanium. Although, most metals display a transition from a continuous chip to a serrated chip with a high enough increase in cutting speed. While it was initially thought that machine-tool vibration was the cause of the serrated chip formation, it has been established in research that the phenomenon is related to the inherent metallurgical features of the work material for the specific machining conditions [50]. Serrated chips do not pose direct negative effects on surface quality; however, it is associated with difficult-to-machine materials, materials which worn out cutting edge quickly.

## 2.7 Summary

Firstly, this thesis chapter presented an extended thick shear zone model for machining processes. The model is based on the work of Pang and Kishawy [34], which assumes that the shear zone is a thick region defined by two parallel sides, with unequal distances from the primary shear zone. The length of the shear line can be calculated as a function of undeformed chip thickness and shear angle. The deformed chip is assumed to have a constant thickness, and shear strain from chip formation can be calculated using the Piispanen Model of Card Analogy. The equivalent shear strain and strain rate can be calculated based on the von Misses yield criterion. The temperature at the shear zone is elevated due to the shearing action, and the normal and friction forces experienced by the tool rake face must be in equilibrium with the shear force and normal force on the shear plane. The hydrostatic stress at two points on the shear plane can be solved, and the total tool-chip contact length can be calculated. There are three variables in the Oxley model that cannot be calculated directly: the primary shear zone thickness ratio, the secondary shear zone (tool-chip interface) thickness ratio, and the shear angle. The optimization search GA and PSO are used to find the solution to these variables such that the solution satisfies three conditions simultaneously: agreement between two methods of calculating normal stress and shear stress on the tool-chip interface, and minimization of cutting force. Secondly, this thesis chapter described the application of the Oxley thick shear zone model to end milling, where the geometry of the tool-workpiece engagement is complex. End milling tools have multiple cutting edges that enter and exit the workpiece periodically with an oblique angle. To calculate cutting forces, the cutting edges are sectioned into disk elements. The cutting force magnitude and direction for each element inside the cut region is calculated and integrated along the cutting edge. The resultant milling forces acting on the tool are the summations of all elemental forces acting on each tooth. The engagement angle of the element is defined by the tool rotation angle and the helix angle of the tooth. If the engagement angle of the element falls within a certain range, the element is engaged with the workpiece and cutting forces are present. The uncut chip thickness of the segment depends on the element engagement angle.

Thirdly, this chapter described the implementation of two optimization algorithms, GA and PSO. GA is an evolutionary algorithm that mimics the natural selection process to find optimal solutions to problems. It involves manipulating a population of chromosomes, each of which encodes the variable values of the problem to be solved. Chromosomes are subjected to fitness evaluations, crossover, and mutation, with better performing chromosomes having a higher chance of crossover to create offspring and pass on their desirable characteristics. Chromosome encoding allows for the manipulation of multiple variables at once, and the fitness evaluation scores the individuals in the population to determine their selection probability. Crossover involves recombining the binary strings of the parents to create offspring, and mutation involves flipping the binary bits of chromosomes. PSO, on the other hand, is a population-based metaheuristic algorithm in which particles move around the solution space based on two parameters, $C_1$ and $C_2$. The cognitive learning factor, $C_1$, gives particles a tendency to move around their personal best solution, while the social learning factor, $C_2$, gives particles a tendency to move closer to the current best solution in the entire population. Velocity, which represents how fast a particle moves through the solution space, is calculated based on the weighting factor, which is high initially to encourage exploration and decreases over time to encourage deeper local search. The objective function for both GA and PSO algorithms is the same, which is a minimization problem.

And finally, this chapter described the four main types of chip formation, chip formation, discontinuous chips, continuous chips, continuous chips with built-up edge (BUE), and serrated chips.

# Chapter 3

# Experimentation

## 3.1 Preamble

This chapter presents the experiments and tests conducted in the course of this thesis. The focus of the research was to compare the mechanical properties and machining behavior of AM metals, specifically titanium Ti-6Al-4V, with wrought metals. To accomplish this, tensile tests and machining tests were conducted on both AM and wrought specimens of titanium Ti-6Al-4V. Hardened steel AISI 4340 and aluminum 6061-T6 were also subjected to machining tests to evaluate the effectiveness of a proposed J-C parameter prediction model on different material types.

The dimensions of the tensile test specimens were based on the ASTM E8/E8M – 13a standard, while the dimensions of the machining blocks varied based on the available materials. Four different mechanical tests were performed to determine the properties of all titanium test materials: tensile tests, hardness tests, SEM imaging, and machining force tests. While machining tests were conducted on hardened steel AISI 4340 and aluminum 6061-T6. The machining experiments, tensile tests, hardness tests, and SEM imaging were conducted using the Haas VF-2YT CNC milling machine, LLOYD LS-100 Plus Universal Testing System, Mitutoyo HR-100, and FlexSEM 1000 respectively.

The cutting forces during machining were monitored using a Kistler 9255C table dynamometer, piezoelectric sensors, and a National Instruments NI USB-6259 DAQ. A CoroMill® 390 square shoulder milling cutter was used for the experiments, and each test was performed using a new insert to minimize the impact of tool wear on the cutting forces. Analyzing the machining of wrought titanium and AM titanium involved 7 machining test sets, with each set involving 9 machining tests at different feeds and speeds. In addition, tests were also conducted on hardened steel and aluminum to further evaluate the proposed J-C parameter prediction model.

The chips and small pieces of titanium were examined using SEM imaging after being cold mounted and etched using hydrofluoric acid. The titanium specimens were manufactured using a Renishaw RenAM 500Q selective laser melting (SLM) metal 3D printing system and were stress relieved after printing to mitigate residual stresses. This chapter provides a comprehensive overview of the experiments and tests conducted in this thesis and sets the stage for the results and discussion presented in subsequent chapters.

## 3.2 Design of Experiment and Experimental Setup

This thesis tested both AM metals as well as wrought metals. For titanium Ti-6Al-4V, both tensile tests and machining tests were conducted on AM and wrought specimens. This is done to compare between the two methods of manufacturing. For hardened steel AISI 4340 steel and aluminum 6061-T6, machining tests were conducted to compare the effectiveness of the proposed J-C parameter prediction model on different material types. Fig. 3.1 showed a recap of the test material types, specimen types, and manufacturing types involved in this thesis.

The tensile test dimensions are based on the ASTM E8/E8M – 13a standard test

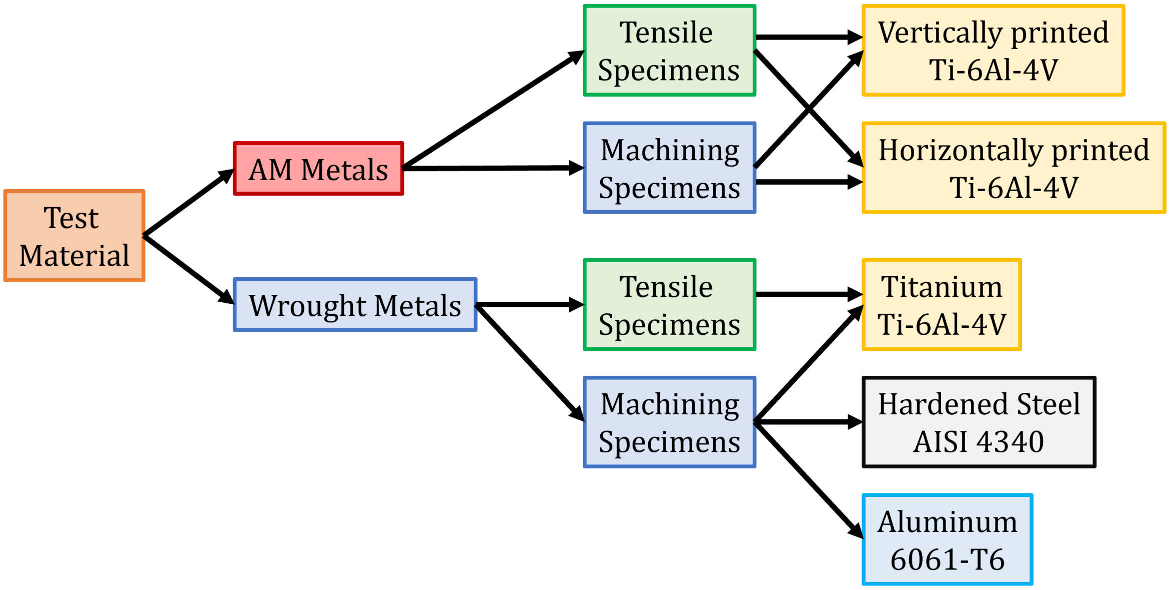

Figure 3.1: Tested AM and wrought metal types

method for tension testing of metallic materials. Specifically, for all AM titanium and wrought titanium tensile specimens, the gauge dimensions are 50 mm length, 12.5 mm width and 5 mm thickness. The dimensions of the machining blocks are different based on the available block materials. In specific, the printed titanium blocks are 100 mm by 30 mm by 30 cm, the wrought titanium blocks are 152 mm by 76 mm by 52 mm, the hardened steel plates are 152 mm by 152 mm by 23 mm, and the aluminum block is 132 mm by 51 mm by 48 mm.

This thesis conducted four different mechanical tests to get the properties of all test materials, as shown in Fig. 3.2. Tensile tests, hardness tests, SEM imaging, and machining force tests are done on both AM and wrought titanium to compare their mechanical properties and machining behaviors. Hardened steel and aluminum only underwent machining tests to examine the effectiveness of the proposed J-C parameter prediction model.

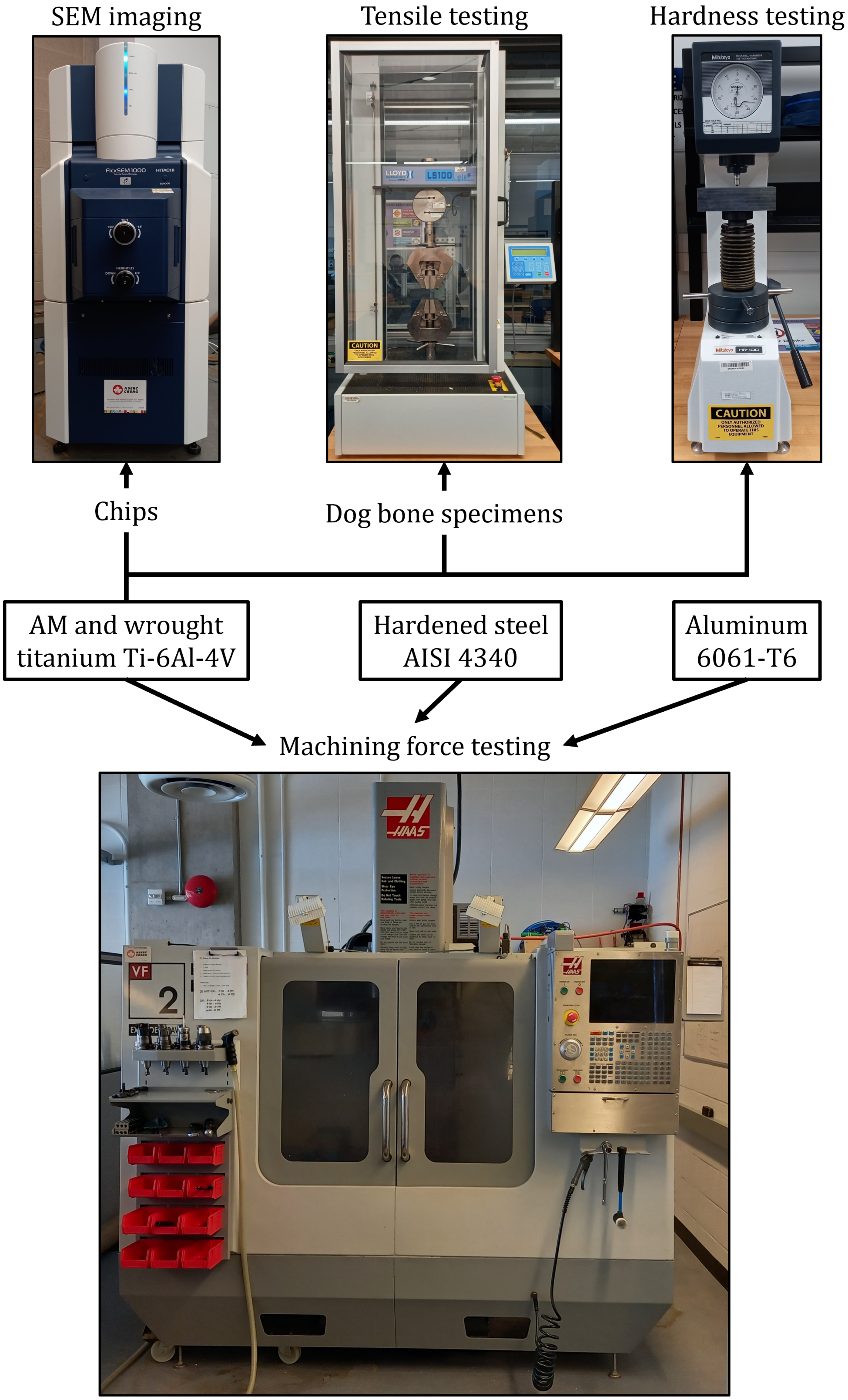

Figure 3.2: Testing types conducted

Machining experiments were conducted using the Haas VF-2YT CNC milling machine. LLOYD LS-100 Plus Universal Testing System was used for tensile testing. Mitutoyo HR-100 was used for hardness testing. FlexSEM 1000 was used to take SEM images of the chips and polished AM titanium pieces.

For all machining tests, the workpiece is clamped on top of the Kistler 9255C table dynamometer. The piezoelectric sensors inside the dynamometer sense the forces in 3 directions, corresponding to the milling machine XYZ directions. Charges are sent through the type 1687B cable to the type 5407A distribution box. The charges corresponding to each axis (X, Y and Z) are distributed to their respective type 5010B charge amplifiers. The amplifiers convert the charge signal into voltage, which is then collected by the National Instruments NI USB-6259 DAQ, converted into digital signal for final processing and recording using a computer, as shown in Fig. 3.3.

CoroMill® 390 square shoulder milling cutter, R390-020A20-11L with R390-11 T3 04M-PM 1130 inserts was utilized to perform the experiments. Each test was done using a new insert to minimize the impact of tool wear on measured cutting forces. Milling tests were conducted using indexable shoulder mills with helical insert instead of end milling to allow inspection and replacement of cutting edge easier and more economical. The helical angle of the insert is a replacement to the helical flute angle of end mills, thus the formulation presented in Chapter 2 is still applicable.

The transducer sensitivity of the charge amplifiers is set to 8.04 pC/MU, and conversion scale of 200 MU/Volt. The force to voltage conversion is shown in Table 3.1.

Contamination due to coolant seeped in between the cable connection on the dynamometer caused some linear drifting in the reported voltage. This was overcome with MATLAB by offsetting the constant linear drift. In addition, environmental noise, such as spindle vibration and atmospheric electromagnetic noise, are partially filtered out using MATLAB Fast Fourier Transform and band-pass filtering.

The tool helix angle and rake angle are measured from the CAD model provided by Sandvik Coromant. The cutting conditions listed in Table 3.2 are applied to all milling tests.

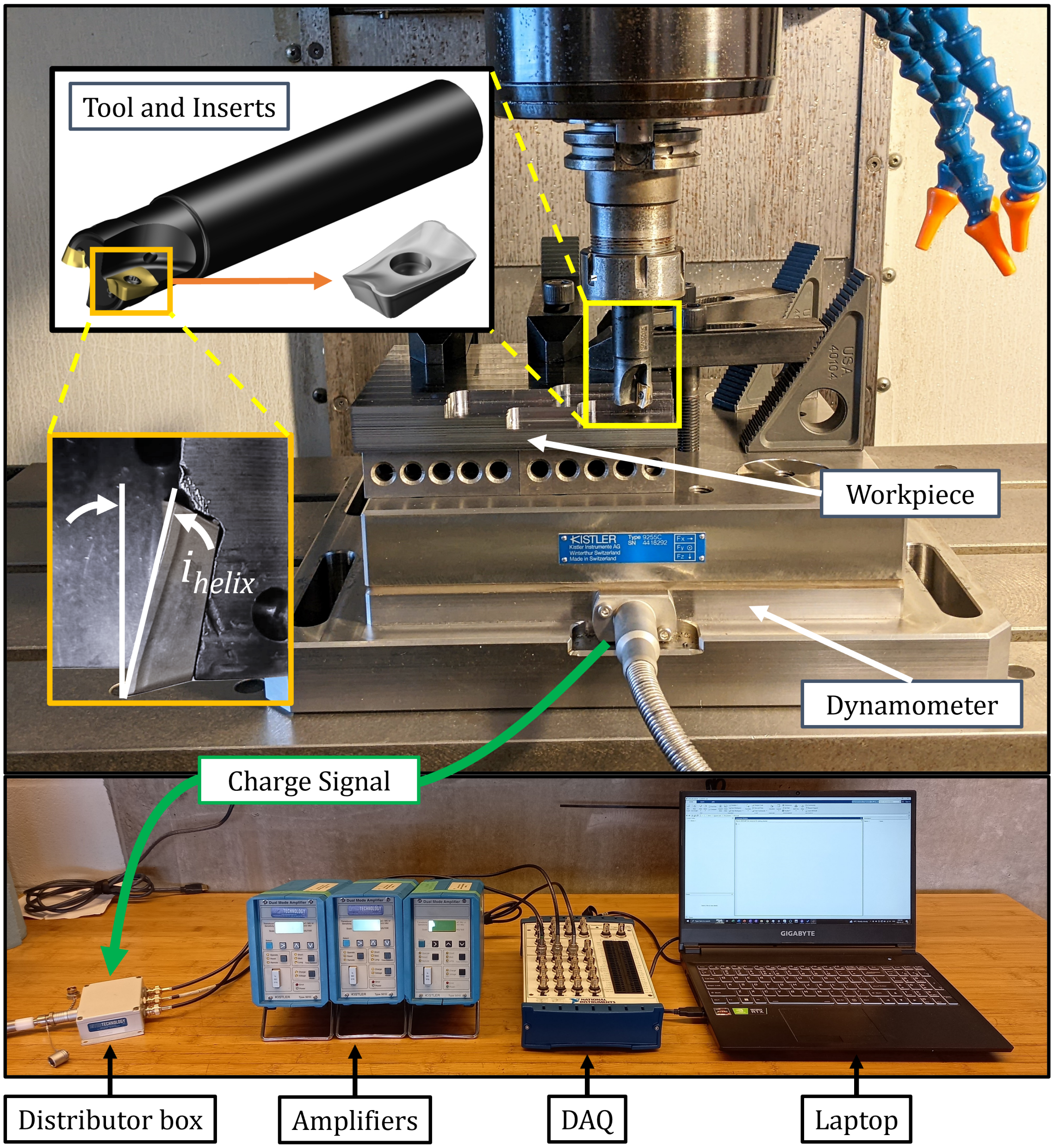

Figure 3.3: Machining force measurement experimental setup

Table 3.1: Voltage to force conversion.

| Axis | X-Axis | Y-Axis | Z-Axis |
|---|---|---|---|
| Conversion Ratio [N/V] | 209.31 | 207.17 | 415.29 |

Table 3.2: Cutting conditions for all milling tests.

| Parameters | Values |
|---|---|
| Cutter diameter | 20 mm |
| Helix angle | 11° |
| Average rake angle | 5° |
| Axial depth of cut | 1 mm |
| Radial depth of cut | 10 mm |
| Cutter entry angle | 90° |
| Cutter exits angle | 180° |
| Workpiece temperature (ambient) | 20°C |

Analyzing and comparing machining of wrought titanium versus AM titanium involves 7 machining test sets, 3 sets for 3 machining directions on the vertically printed specimen, 3 sets for 3 machining directions on the horizontally printed specimen, and 1 set for machining on the wrought titanium. Wrought titanium is known to be isotropic so only one set of machining test is required. Each machining set involves 9 machining tests with different feeds and speeds as shown in Table 3.3. Nominal feeds and speeds (100% speed and 100% feed) are recommended values from Sandvik Coromant. Titanium is very difficult to machine due to its high hardness, strength, tendency to work harden, and most importantly, high heat generation with low thermal conductivity. Therefore, all tests on titanium are done with coolant to minimize the effects of tool wear. Titanium tests are done with only 1 insert installed to eliminate the effect of tool run-out.

In addition to titanium machining tests, 1 set of 4 machining tests is done on hardened steel AISI 4340, and 1 set of 3 machining tests is done on aluminum 6061-T6 to further analyse the strengths and weaknesses of the proposed J-C parameter prediction model, as listed in Table 3.4. These tests are done with dry machining as the tool wear rate is less of a concern than titanium. Furthermore, these tests are done with both inserts installed to examine the effects of tool run-out on the prediction quality.

Table 3.3: Feeds and speeds for AM and wrought titanium machining tests.

| | | 70% Speed | 100% Speed | 130% Speed |
|---|---|---|---|---|
| 70% Feed | Surface speed | 35 m/min | 50 m/min | 65 m/min |
| | Feed per tooth | 0.07 mm/tooth | 0.07 mm/tooth | 0.07 mm/tooth |
| 100% Feed | Surface speed | 35 m/min | 50 m/min | 65 m/min |
| | Feed per tooth | 0.10 mm/tooth | 0.10 mm/tooth | 0.10 mm/tooth |
| 130% Feed | Surface speed | 35 m/min | 50 m/min | 65 m/min |
| | Feed per tooth | 0.13 mm/tooth | 0.13 mm/tooth | 0.13 mm/tooth |

Chips and small pieces of titanium are examined using SEM imaging. Some are cold mounted to aid with the analysis process as shown in Fig. 3.4. The chips were collected after the machining tests. The small titanium pieces were obtained by using wire EDM to cut the corners of the printed machining blocks. The cold mounting process involves submerging the samples in epoxy resin that slowly solidifies at room temperature. The cured cylindrical samples are hand ground into close shape, then automatically ground and polished using the Struers Tegramin 25 to obtain a perfectly flat surface. Finally, the samples are cleaned and etched using hydrofluoric acid (HF) to increase exposed metal contrast under SEM imaging.

Table 3.4: Feeds and speeds for hardened steel AISI 4340 and aluminum 6061-T6 tests.

| | | Hardened Steel AISI 4340 | Aluminum 6061-T6 |
|---|---|---|---|
| Test 1 | Surface speed | 60 m/min | 100 m/min |
| | Feed per tooth | 0.10 mm/tooth | 0.06 mm/tooth |
| Test 2 | Surface speed | 100 m/min | 50 m/min |
| | Feed per tooth | 0.10 mm/tooth | 0.12 mm/tooth |
| Test 3 | Surface speed | 100 m/min | 100 m/min |
| | Feed per tooth | 0.15 mm/tooth | 0.06 mm/tooth |
| Test 4 | Surface speed | 125 m/min | |
| | Feed per tooth | 0.20 mm/tooth | |

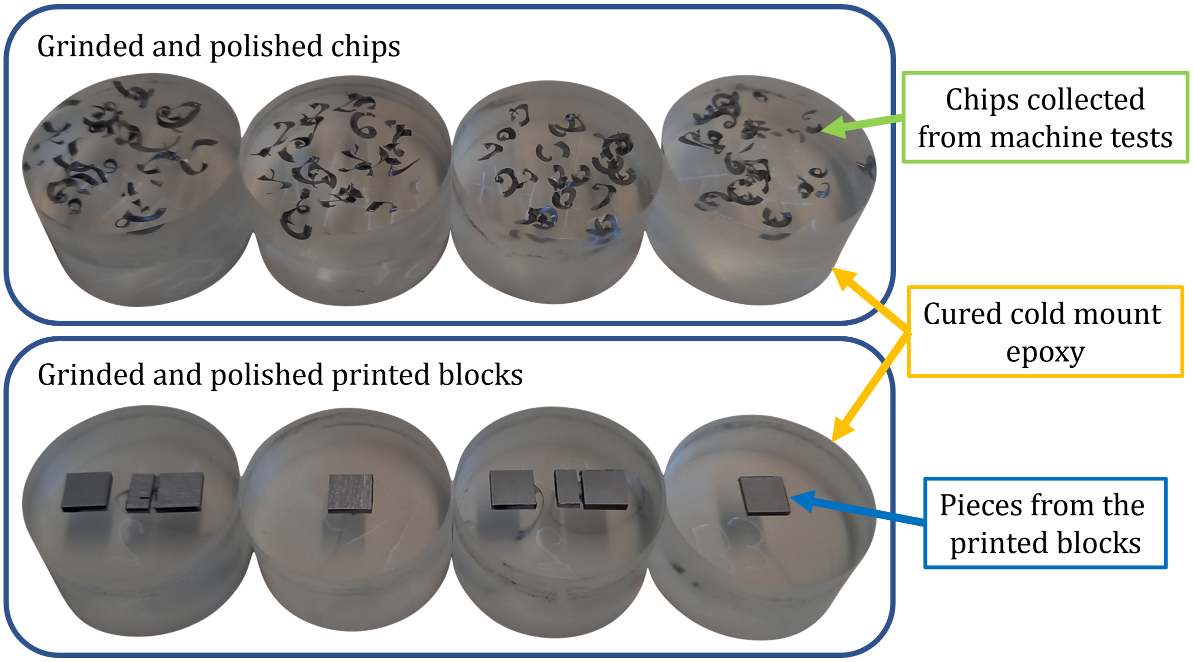

Figure 3.4: Cold mounted samples for AM and wrought titanium chips from machining tests and pieces from machining blocks

## 3.3 Additive Manufactured Metal Parts

The RenAM 500Q selective laser melting (SLM) metal 3D printing system was used to manufacture the titanium Ti-6Al-4V specimens for tensile and machining experiments. Titanium powder was melted and fused locally layer-by-layer to form fully dense (100% infill) parts. The process of heating, melting, and cooling occurs very quickly, which leads to the creation of residual stresses. To mitigate these stresses, the parts were stress relieved in an Argon atmosphere after the printing process. The printer was capable of printing parts in both the vertical and horizontal orientations. For this study, 6 tensile test specimens (3 horizontally and 3 vertically) along with 2 machining blocks (1 horizontal and 1 vertical) were printed, as shown in (a). Three machining directions are examined to investigate if there is any difference in cutting forces versus printing direction, as shown in Fig. 3.5(d).

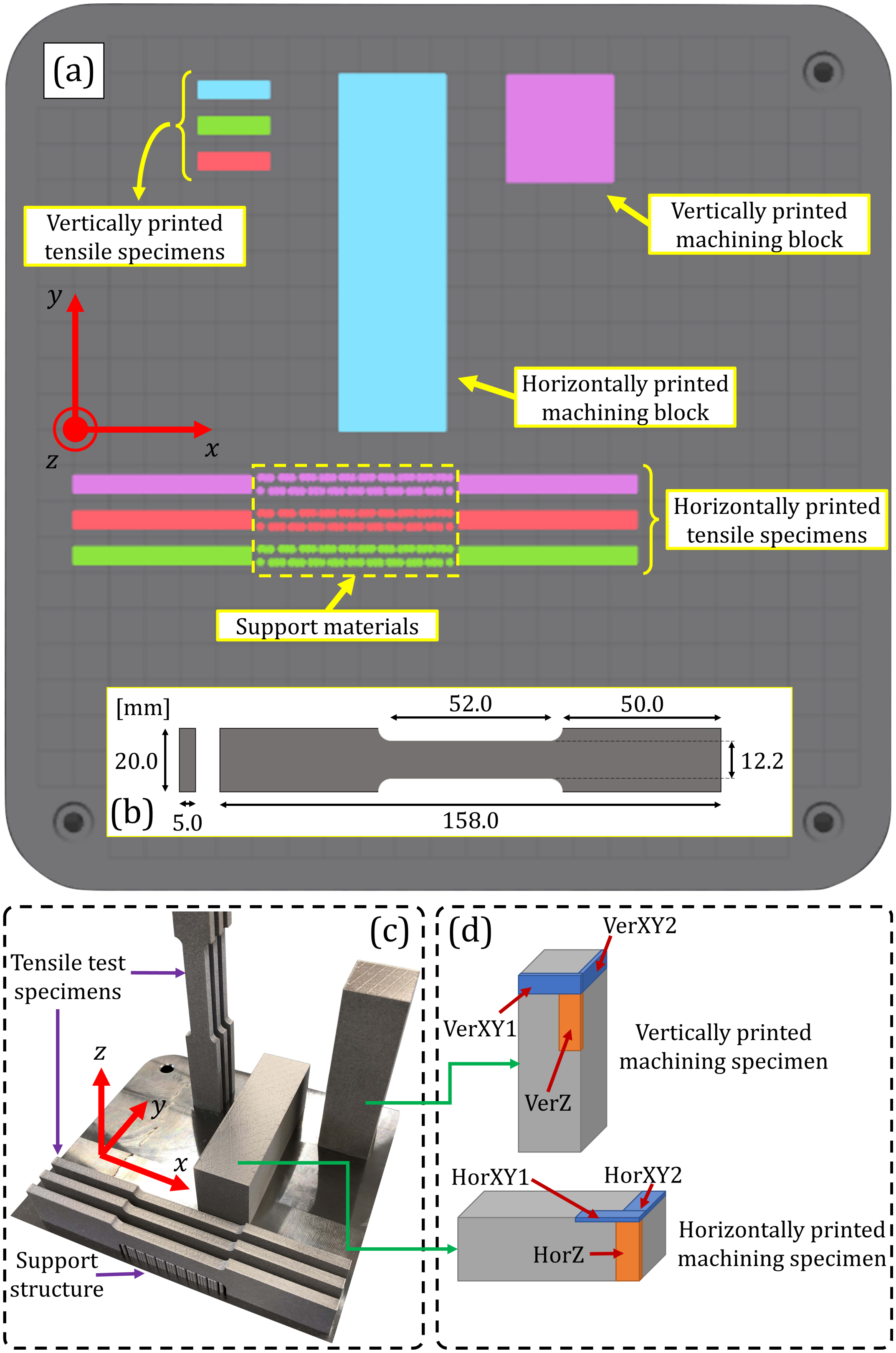

Figure 3.5: (a) Metal printing setup, (b) tensile test dimensions, (c) printed parts and (b) machining direction versus printing direction.

## 3.4 Summary

This chapter described the experiments and tests which were conducted. The test metals included wrought and AM titanium Ti-6Al-4V, wrought hardened steel AISI 4340, and wrought aluminum 6061-T6. The purpose of these tests was to compare the mechanical properties and machining behaviors of the metals manufactured through AM methods versus wrought methods, in additional to testing the proposed J-C determination model. The experiments included tensile tests, hardness tests, SEM imaging, and machining force tests. The tensile test dimensions followed the ASTM E8/E8M – 13a standard, while the machining tests were performed using a Haas VF-2YT CNC milling machine. The RenAM 500Q SLM metal 3D printing system was used to manufacture all AM titanium specimens. The results of the tests were analyzed using MATLAB, and SEM imaging was used to examine the chips after the machining test, as well as small pieces of titanium obtained by wire EDM cutting. The results of the tests were used in the next chapter to evaluate the effectiveness of the proposed J-C parameter prediction model on different metals.

# Chapter 4

# Results and Discussion

## 4.1 Preamble

This chapter presented results from experiments and tests to be used by the proposed J-C parameters determination model. The content is divided into two main sections, with the first section focusing on the testing of the efficacy of the model using experiments on hardened steel AISI 4340 and aluminum 6061-T6. In this section, experiments were performed to search for the J-C parameters by selecting three different angular positions (reference positions for reference forces) of the tool and their corresponding force components in the X and Y directions. The reference forces were selected to reduce the computational load on the algorithm, while still maintaining the accuracy of the results. The results for aluminum 6061-T6 varied from the values found in open literature, likely due to small discrepancies in the characteristics of the material from different batches or different vendors. The resulting J-C parameters from the GA and PSO search were validated by using Oxley PSO to predict the cutting forces and comparing them to the measured cutting forces. The results showed good agreement for AISI 4340 hardened steel, but a lower agreement for aluminum 6061-T6, likely due to the unstable and unpredictable measured cutting forces. PSO was shown to have slightly faster convergence to optimal J-C parameters than GA, thus it was used as the optimization method for the J-C search of AM titanium. The second section focuses on investigating the differences between machining wrought and AM titanium Ti-6Al-4V. Tensile tests were carried out to evaluate the mechanical properties of titanium Ti-6Al-4V and the quasi-static J-C parameters were obtained from true stress-strain data. The tensile tests results showed that wrought Ti-6Al-4V exhibited the highest ductility, while the vertically printed AM specimens had the highest ultimate strength. The higher hardness readings of the AM titanium were due to the AM process, which increased the hardness and brittleness of the material. The results showed that wrought titanium had the lowest cutting forces, while both feed and cutting speed increases the cutting forces for AM titanium much quicker than wrought titanium. The machining of both wrought and AM titanium produced saw-toothed chips due to the adiabatic shear in the primary shear zone. The shear band thickness of both AM and wrought titanium was almost similar, but the shear bands in AM titanium appeared to be more pronounced and penetrated deeper into the chip.

## 4.2 Validating the J-C Determination Model for Hardened Steel AISI 4340 and Aluminum 6061-T6

Machining experiments were performed on AISI 4340 hardened steel (47±1 Rockwell hardness C), and Aluminum 6061-T6. The quasi-static J-C parameters A, B and n were obtained from open literature. The remaining two J-C parameters C and m, along with thermal coefficient $\eta$ and $\psi$, were considered as unknown and were searched. The relevant material properties of AISI 4340 hardened steel and Aluminum 6061-T6 are listed in Table 4.1. In order to search for the J-C parameters,

Table 4.1: Material properties of hardened steel AISI 4340 and aluminum 6061-T6.

| Parameters | Hardened steel AISI 4340 | Aluminum 6061-T6 |
|---|---|---|
| Density, $g/cm^3$ | 7.85 | 2.7 |
| Heat capacity, $J/g \cdot^{\circ} C$ | 0.475 | 0.896 |
| Thermal conductivity, $W/m \cdot K$ | 44.5 | 167 |
| Melting temperature, $^{\circ}C$ | 1427 | 582 |
| Yield stress ($A$), MPa | 950 [1] | 324 [3] |
| Strength coefficient ($B$), MPa | 725 [1] | 114 [3] |
| Strain hardening exponent ($n$) | 0.375 [1] | 0.420 [3] |

three different angular positions of the tool during one full rotation were selected as the reference angles and their corresponding force components in the X and Y direction is used. In theory, these force components could be selected from every force direction e.g., X, Y, and Z and the number of reference angles can be any arbitrarily selected value. Using more reference angles for more force directions would allow for better J-C parameter estimation. However, calculating forces from the Oxley model is computationally expensive. In addition, the method presented in this thesis requires dividing the cutting edge into many small elements; in addition, GA and PSO require the calculation of cutting forces for each individual chromosome in the population, and for the entire population for every iteration. Therefore, to keep the algorithm computationally efficient and responsive, the number of sampling points must be kept minimal. To achieve this, average reference forces along X and Y direction at 20°, 60°, and 80° angular positions during one full rotation of the tool were selected such that they covered a wide span of high to low cutting forces.

For the AISI 4340 hardened steel, the run-out was approximately zero, while for Aluminum 6061-T6, the tool run out was approximately 0.05 mm between the two inserts of the shoulder mill. The run-out was measured using a dial indicator before each test. Due to the presence of run-out, the cutting forces between the two inserts were not entirely identical. To improve search results, the average value of cutting forces between the two inserts were used, as mentioned in Table 4.2 and Table 4.3.

In addition, tests with different feed per tooth (FPT) and surface speed (SFM) were conducted to ensure the validity of results for a wide range of cutting conditions. As previously stated, these specific reference forces were used only to reduce the computational load on the algorithm without jeopardizing the accuracy of the results. For AISI 4340 hardened steel, four tests were performed in total. Two of them were used to calibrate the model by extracting the J-C parameters, and to validate the model. The other two tests were solely performed for validating the model. These

Table 4.2: Reference forces from AISI 4340 hardened steel tests.

| Reference angles | FPT 0.1 mm, SFM 60 mm/min | | FPT 0.2 mm, SFM 125 mm/min | |
|---|---|---|---|---|
| | $F_X$ (N) | $F_Y$ (N) | $F_X$ (N) | $F_Y$ (N) |
| 20° | 105 | 360 | 150 | 580 |
| 60° | -95 | 280 | -130 | 450 |
| 80° | -95 | 140 | -130 | 250 |

Table 4.3: Reference forces from Aluminum 6061-T6 tests.

| Reference angles | FPT 0.12 mm, SFM 100 mm/min | | FPT 0.06 mm, SFM 100 mm/min | | FPT 0.12 mm, SFM 50 mm/min | |
|---|---|---|---|---|---|---|
| | $F_X$ (N) | $F_Y$ (N) | $F_X$ (N) | $F_Y$ (N) | $F_X$ (N) | $F_Y$ (N) |
| 20° | 90 | 320 | 70 | 220 | 100 | 310 |
| 60° | -70 | 250 | -40 | 160 | -85 | 230 |
| 80° | -60 | 130 | -45 | 80 | -70 | 120 |

two tests were not initially used in calibrating the model to ensure that the extracted J-C parameters were still valid. Three tests were performed for Aluminum 6061-T6 each, all for both calibration and validation. Using different number of tests in the search allowed for the investigation of number of tests required for J-C searches.

As mentioned before, the Oxley search is nested inside J-C search; therefore, their search parameters can be different if desired. The search parameters shown in Table 4.4 and Table 4.5 are chosen from general rules of thumb and best practices available in the open literature [52]. J-C search population size was chosen to be at 60 to maximizes the utilization of CPU cores. The CPU used for this simulation was an AMD Ryzen™ Threadripper™ PRO 3955WX with 16 cores.

The variable ranges for J-C parameters C and m and thermal coefficient $\eta$ and $\psi$ are listed in Table 4.6. This is a reasonable guess range based on previously established J-C parameters for AISI 4340 hardened steel, Titanium Ti-6Al-4V, Aluminum 6061-T6, and other metals in general. For the Oxley GA search, $\phi_c$ is set to be less than 45° because produced chip will always be thicker than uncut chip. Shear zone thickness $C_0$ and $\delta$ are set to a reasonable range proposed in open literature, see Table 4.6.

Table 4.4: GA search parameters.

| Parameters | J-C Search | Oxley Search |
|---|---|---|
| Population size | 60 | 100 |
| Crossover rate | 90% | 90% |
| Mutation rate | 5% | 5% |
| Elite percentage | 5% | 5% |
| Stop condition | 50 generations | 120 generations |
| Number of binary bits per variable | 20 bits | 20 bits |

Table 4.7 summarize and compare the C and m values found by the proposed method

Table 4.5: PSO search parameters.

| Parameters | J-C Search | Oxley Search |
|---|---|---|
| Population size | 60 | 100 |
| Cognitive learning factor, $C_1$ | 2.05 | 2.05 |
| Social learning factor, $C_2$ | 2.05 | 2.05 |
| Maximum weighting | 0.9 | 0.9 |
| Minimum weighting | 0.4 | 0.4 |
| Stop condition | 50 generations | 120 generations |

Table 4.6: Variable ranges.

| Range of Parameters | Values |
|---|---|
| $C$ (J-C search) | 0 to 0.1 |
| $m$ (J-C search) | 0 to 2 |
| $\eta$ (J-C search) | 0 to 1 |
| $\psi$ (J-C search) | 0 to 1 |
| $\phi$ (Oxley search) | 5° to 45° |
| $C_0$ (Oxley search) | 2 to 10 |
| $\delta$ (Oxley search) | 0.005 to 0.2 |

in this thesis vs. those that are presented in open literature.

To ensure the consistency of the calculated J-C parameters, GA and PSO were repeated three times for each workpiece materials, as shown in Fig. 4.1. The accuracy of GA and PSO in searching for J-C parameters can be evaluated by comparing the calculated force to the experimentally measured ones. This can be achieved using the sum of the errors between the calculated and measured forces, which is known as fitness score. Lower fitness score indicates better force predictions. As can be seen in Fig. 4.1, PSO converges to more accurate solutions comparing to GA. PSO also exhibits less fluctuation during the search process which translates into a more accurate prediction of J-C parameters for a certain number of iterations. The calculated J-C parameters ($C$, $m$) and thermal coefficients ($\eta$, $\psi$) using GA and PSO after 50 iterations are listed in Table 4.8.

The results for AISI 4340 hardened steel showed good agreement with the already published values in open literature. Strain rate hardening was found to be between 0 and 0.0059, which is expected as hardened steel does not exhibit high strain rate

Table 4.7: Johnson-Cook model constants from this thesis compared with open literature.

| Source | Material | $C$ | $m$ | Method |
|---|---|---|---|---|
| This thesis using GA | AISI 4340 (Hardened) | 0.0059 | 0.929 | Quasi-static tensile tests and end milling tests |
| This thesis using PSO | AISI 4340 (Hardened) | 0.0000 | 1.146 | Quasi-static tensile tests and end milling tests |
| Eu-Gene et al. [1] | AISI 4340 (Hardened) | 0.015 | 0.625 | Finite element simulations |
| Johnson et al. [53] | AISI 4340 | 0.014 | 1.03 | Torsion tests, Hopkinson bar tests, and quasi-static tensile tests |
| Chandrasekaran et al. [54] | SS2541 (Equivalent to AISI 4340) | 0.072 | 0.513 | Hopkinson bar tests and orthogonal cutting tests |
| This thesis using GA | Aluminum 6061-T6 | 0.0994 | 1.893 | Quasi-static tensile tests and end milling tests |
| This thesis using PSO | Aluminum 6061-T6 | 0.1000 | 2.000 | Quasi-static tensile tests and end milling tests |
| Lesuer et al. [3] | Aluminum 6061-T6 | 0.002 | 1.34 | Hopkinson bar tests |

Table 4.8: J-C and thermal coefficient results from GA and PSO.

| Material | Algorithm | $C$ | $m$ | $\eta$ | $\psi$ |
|---|---|---|---|---|---|
| AISI 4340 (hardened) | GA | 0.0059 | 0.929 | 0.960 | 0.554 |
|  | PSO | 0.0000 | 1.146 | 1.000 | 0.560 |
| Aluminum 6061-T6 | GA | 0.0994 | 1.893 | 0.113 | 0.742 |
|  | PSO | 0.1000 | 2.000 | 0.038 | 0.879 |

hardening property. Thermal softening exponent for AISI 4340 hardened steel was found to be between 0.929 and 1.146 compared to 0.513 from Chandrasekaran et al. [54], 1.03 from Johnson et al. [53], and 0.625 from Eu-Gene et al [1]. For aluminum, the C and m values found in this study varied from the values found by Lesuer et al. [3]. This is likely because although the A, B, and n values used in the model were taken from open literature for the same Al 6061, there might still be small discrepancies due to characteristics variations among the batches produced by different vendors or even the same vendor at different times. In addition, the reference cutting forces for aluminum were found to be unstable, likely due to the sticky nature of aluminum, as shown in Fig. 4.4 and Fig. 4.5.

To validate the resulting $C$, $m$, $\eta$, and $\psi$ values from the GA and PSO search, Oxley PSO is used once again to predict the cutting force generated and then to compare them with the measured cutting forces at different cutting conditions, see Fig. 4.2 to Fig. 4.5. The predicted cutting forces for AISI 4340 hardened steel showed a good agreement with the measured cutting forces. However, predicted cutting forces for Aluminum 6061-T6 and titanium Ti-6Al-4V showed a lower agreement to measured cutting forces, mainly due to the unstable and unpredictable measured cutting forces. It must be noted that J-C search results are highly dependent on the quality of the measured cutting forces and the stability of the cuts; thus, when measured forces

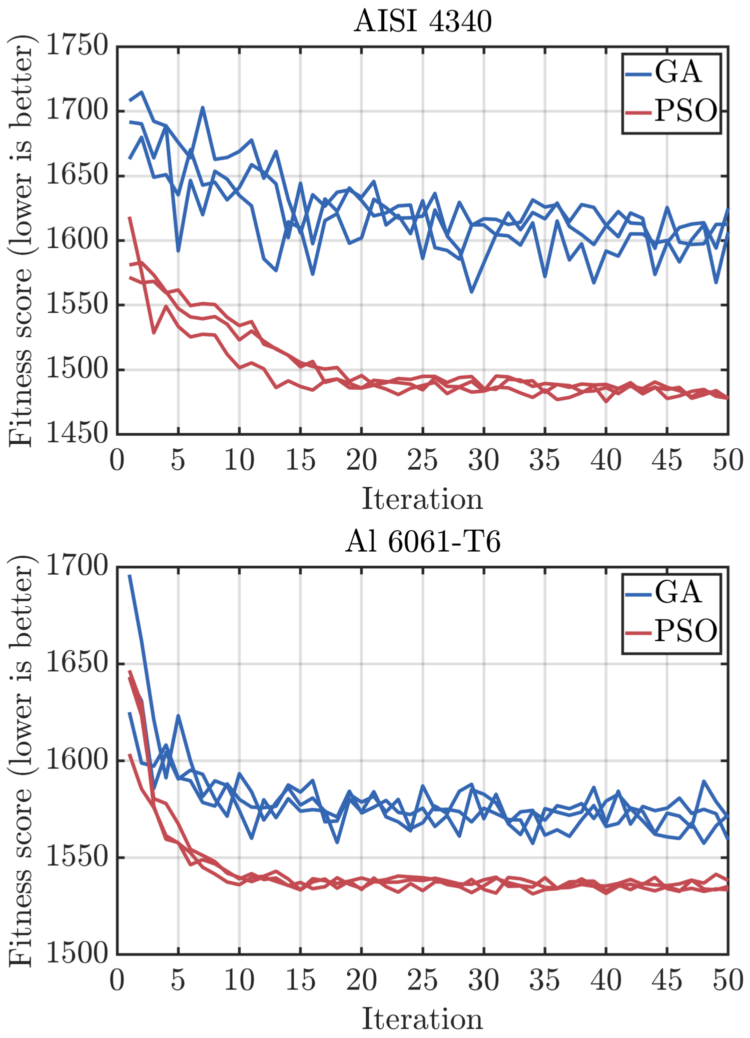

Figure 4.1: Convergent speed and fitness quality of GA vs. PSO for hardened steel AISI 4340 and aluminum Al 6061-T6.

are unstable and fluctuating, the accuracy of the model will be affected. Analyzing the cutting data revealed that measured cutting force profiles of Aluminum 6061-T6 exhibit unstable behavior, specifically unpredictable large fluctuations when the tool is not in cut, see the area between 90° and 180° as well as the area between 270° and 360°, see Fig. 4.4 and Fig. 4.5.

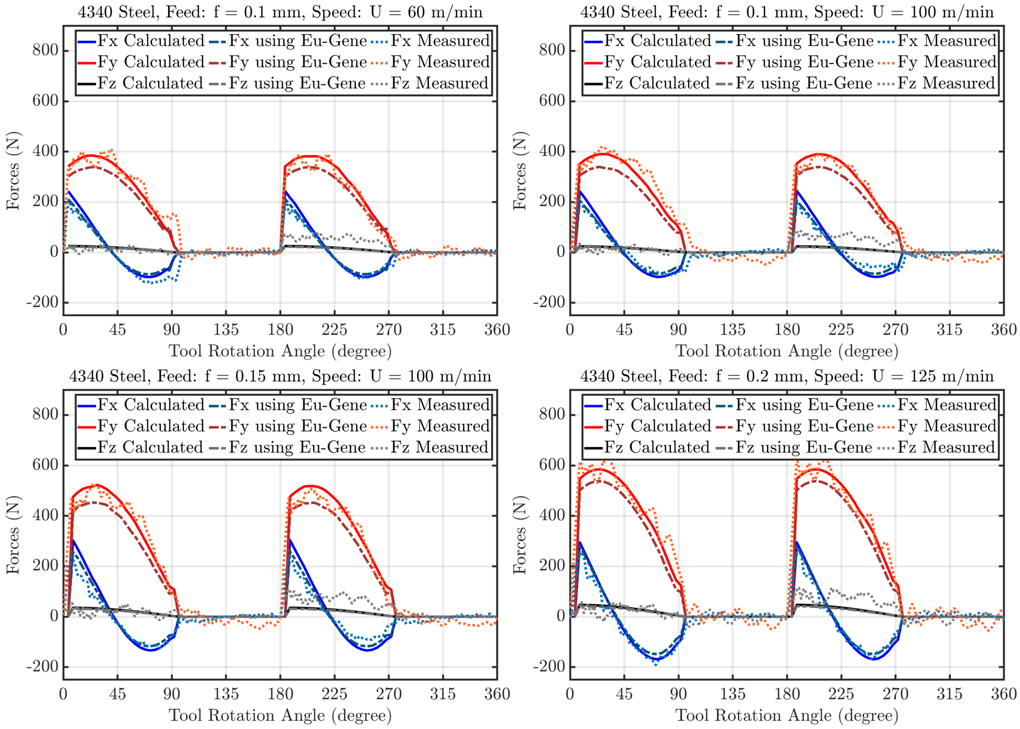

Figure 4.2: Cutting force prediction using J-C results from Eu-Gene [1], versus from this thesis using GA, and versus measured for hardened steel AISI 4340. [2]

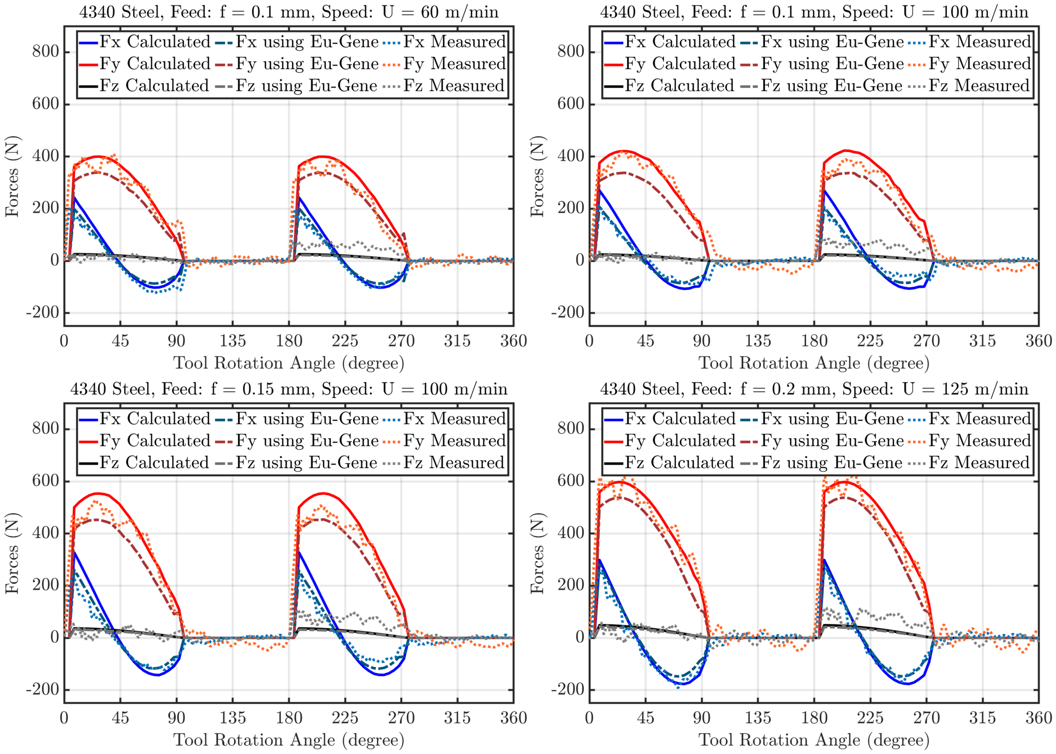

Figure 4.3: Cutting force prediction using J-C results from Eu-Gene [1], versus from this thesis using PSO, and versus measured for hardened steel AISI 4340. [2]

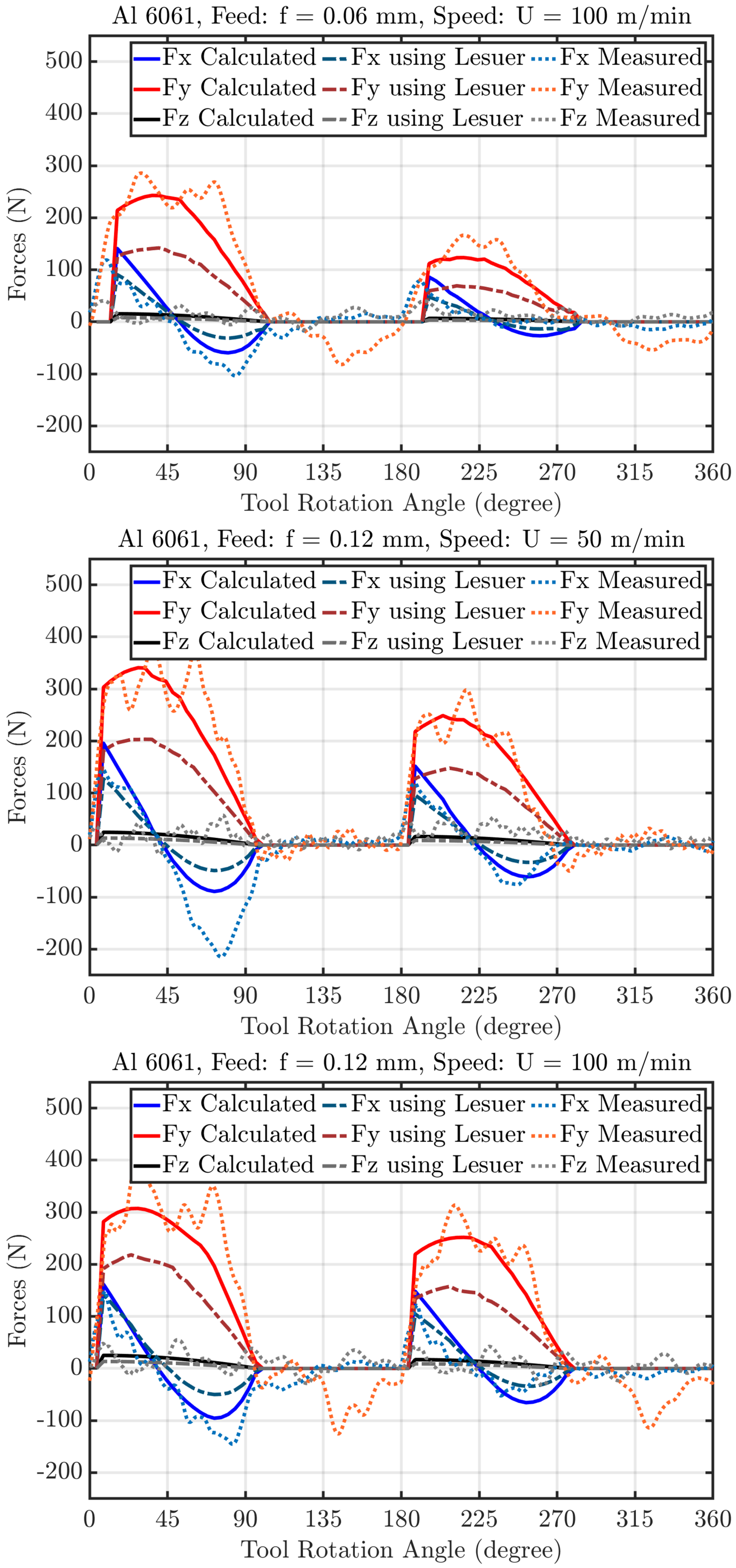

Figure 4.4: Cutting force prediction using J-C results from Lesuer [3], versus from this thesis using GA, and versus measured for aluminum 6061-T6. [2]

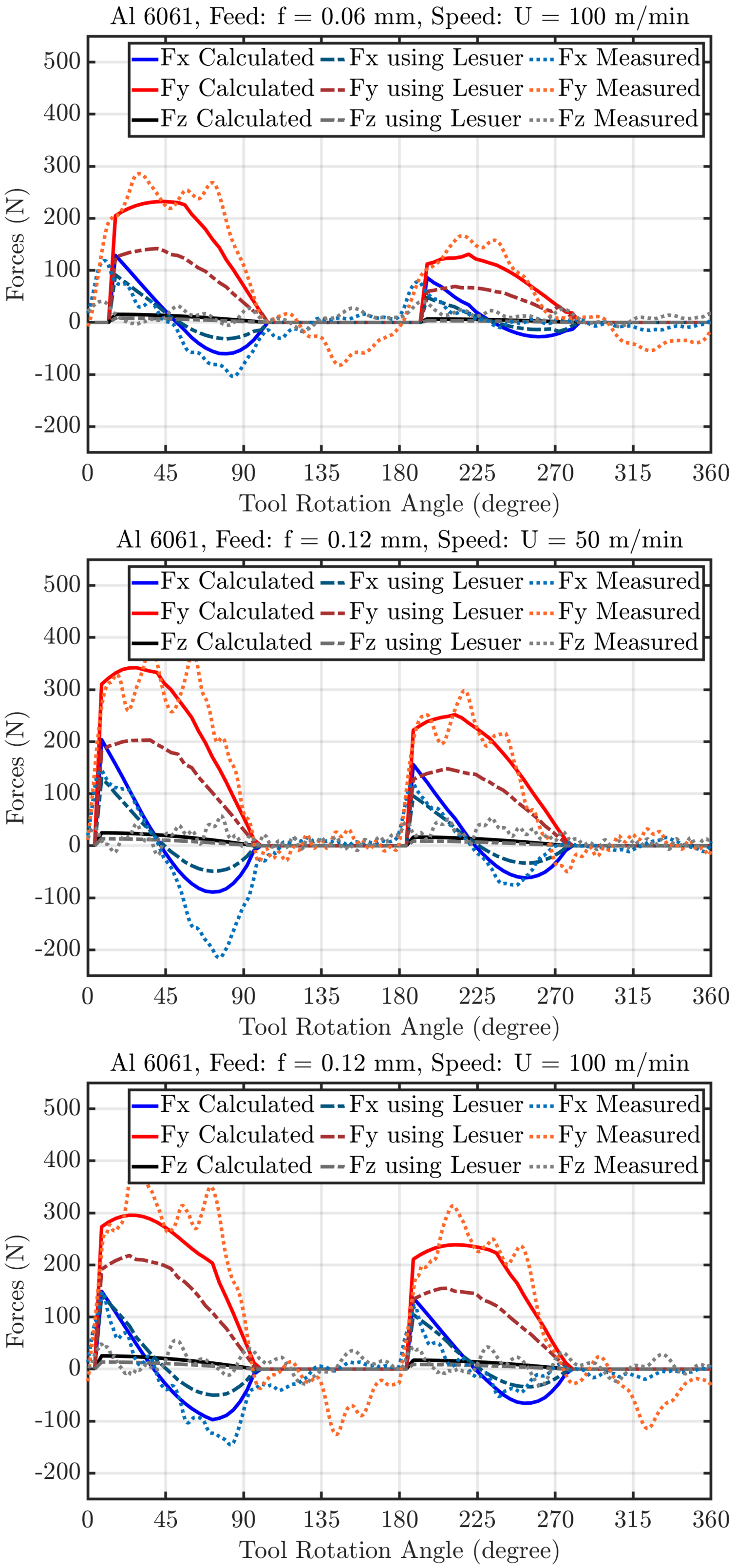

Figure 4.5: Cutting force prediction using J-C results from Lesuer [3], versus from this thesis using PSO, and versus measured for aluminum 6061-T6. [2]

## 4.3 Implementing Search Model on Wrought and AM Titanium Ti-6Al-4V

### 4.3.1 Tensile Test Results

As stated in the previous chapter, tensile tests were carried out to evaluate the mechanical properties of titanium Ti-6Al-4V. A total of 9 tensile tests were performed, including 3 specimens fabricated using the wrought method, 3 specimens were printed in the vertical orientation and the remaining 3 in the horizontal orientation. As opposed to obtaining the quasi-static J-C parameters A, B, and n from open literature, these parameters for all titanium materials are obtained from true stress-strain data from tensile tests. These results are reported in Table 4.9. Since horizontally printed titanium exhibited brittle fracture as shown in Fig. 4.6, their B and n values could not be obtained from their tensile tests. Thus, these parameters were included in the PSO model and searched.

The results showed that all 9 specimens demonstrated a similar behavior in the elastic region, however, deviation was observed when entering the plastic region as

Table 4.9: Quasi-static J-C parameters results from tensile tests.

| Direction | A (MPa) | B (MPa) | n |
|---|---|---|---|
| Wrought | 1038 | 401.5 | 0.473 |
| AM VerXY1 | 1093 | 690.8 | 0.389 |
| AM VerXY2 | 1093 | 701.1 | 0.418 |
| AM VerZ | 1093 | 777.8 | 0.372 |
| AM HorXY1 | 1062 | Included in J-C search | Included in J-C search |
| AM HorXY2 | 1062 | Included in J-C search | Included in J-C search |
| AM HorZ | 1062 | Included in J-C search | Included in J-C search |

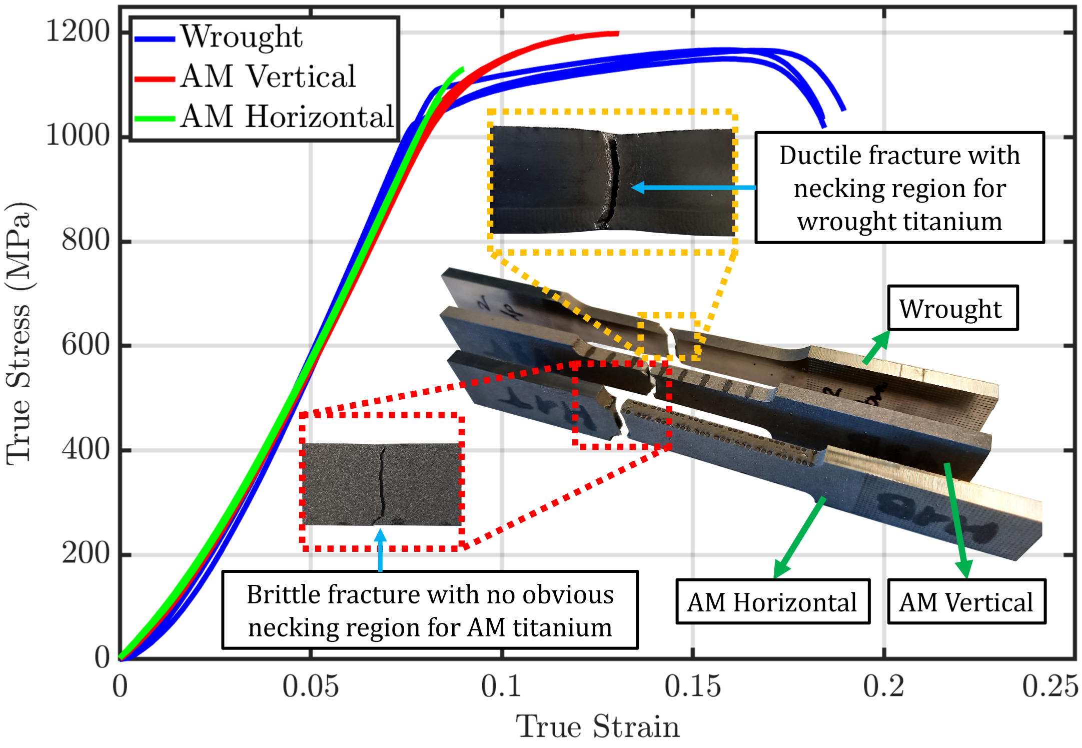

Figure 4.6: Tensile test results for wrought and AM Ti-6Al-4V. [4]

shown in Fig. 4.6. Specifically, the wrought Ti-6Al-4V specimens displayed the highest ductility among all the specimens tested. On the other hand, the ultimate strength was found to be the highest in the vertically printed AM specimens. Conversely, the horizontally printed AM specimens exhibited a brittle fracture behavior.

### 4.3.2 Hardness Test Results

To better understand the different behavior of wrought and AM Ti-4Al-6V, their hardness was measured using Mitutoyo HR-100 hardness tester at 5 different locations on the corresponding machining blocks and the average values are presented in Table 4.10.

The higher hardness readings of the AM titanium are the inevitable result of the AM process in which a beam of laser rapidly sinters the powder. In this process, the material locally melts and instantly solidifies which ultimately increases the hardness and makes the material more brittle.

Table 4.10: Hardness values for wrought and AM Ti-4Al-6V.

| Wrought | AM Vertical | AM Horizontal |
|---|---|---|
| 43±0.5 HRC | 48±0.5 HRC | 48±0.5 HRC |

### 4.3.3 Cutting Forces and J-C Parameters Results

The chosen optimization method for searching J-C parameters of wrought and AM titanium is PSO. From previous results for hardened steel AISI 4340 and aluminum 6061-T6, PSO has shown to be able to converge faster than GA, while the final results for both GA and PSO are similar. Employing J-C search using PSO for all titanium samples also requires the fundamental material properties of titanium, as listed in Table 4.11. The required quasi-static values are listed above in the sub section 4.3.1 in Table 4.9.

To compare the cutting forces, the peak resultant forces for each of the 63 scenarios

Table 4.11: Known material properties of titanium Ti-6Al-4V.

| Parameters | Titanium Ti-6Al-4V |
|---|---|
| Density, $g/cm^3$ | 4.43 |
| Heat capacity, $J/g \cdot^\circ C$ | 0.5263 |
| Thermal conductivity, $W/m \cdot K$ | 6.7 |
| Melting temperature, $^\circ C$ | 1660 |

(54 AM and 9 wrought) were presented in Fig. 4.7. As can be seen, wrought titanium exhibited the lowest cutting force across all cutting conditions. At feed rate of 0.07 mm per tooth, AM titanium produced similar cutting forces to the wrought one. However, as feed increased, machining AM blocks generated higher cutting forces. An expected trend can be observed when machining wrought titanium where cutting forces increased as feed increased ( 20.1% increase in force per 0.03 mm increase in feed). However, increasing cutting speed did not significantly contribute to increase the force values. In contrast, when machining AM titanium, both feed and cutting speed were found to be impactful on cutting forces ( 29.1% increase in force per 0.03 mm increase in feed, 7.2% increase in force per 15 m/min increase in speed). Notably, cutting forces increased at 65 m/min for some AM tests ( 30.8% higher peak force). This sudden increase in cutting forces can be attributed to the higher hardness of AM titanium, which also led to substantial tool wear.

The process of determining the remaining J-C parameters $C$ and $m$ for all cutting

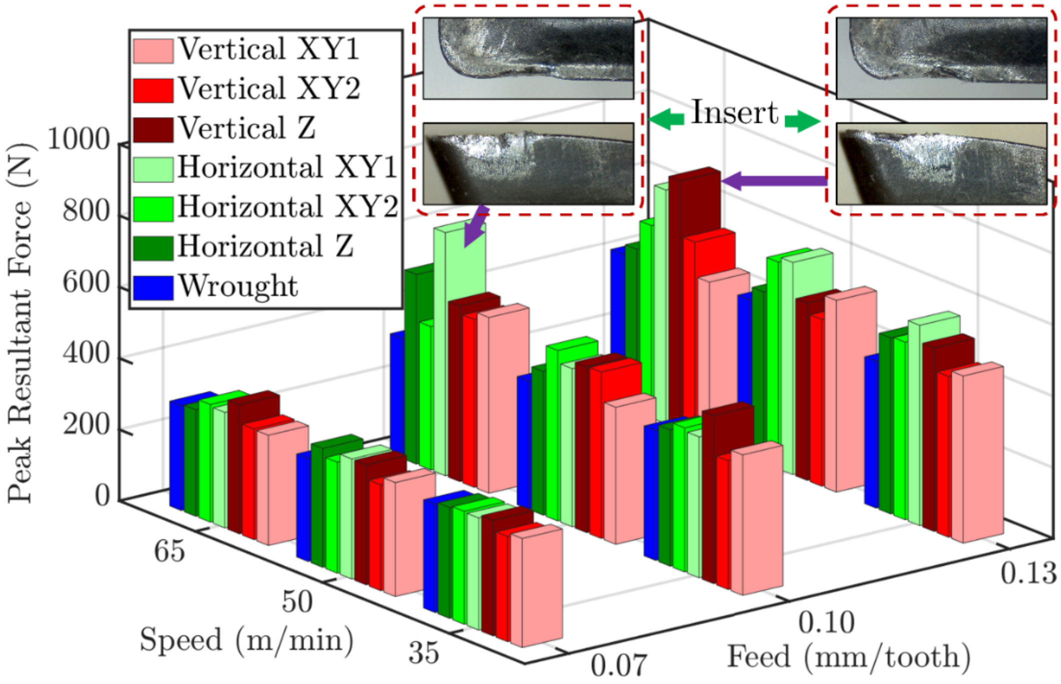

Figure 4.7: Measured peak cutting force for different feeds and speeds, along different machining directions versus printing directions. [4]

directions are similar to the process applied to hardened steel AISI 4340 and aluminum 6061-T6. For each cutting direction, cutting forces produced from four sets of feeds and speeds were used as training data (0.07 mm and 35 m/min; 0.07 mm and 65 m/min; 0.10 mm and 50 m/min; 0.13 mm and 35 m/min). These sets were chosen as they were among the least affected by tool wear. The resulting C and m values are presented in the Table 4.12.

The model was successful at predicting the required J-C parameters, even when $B$ and $n$ were missing for horizontally printed titanium. This demonstrated the robustness and versatility of the model in handling various input scenarios. Even though $C$ values varied between the cutting directions, they were all consistently high, which matched with the expectation that titanium can maintain its strength and toughness at high strain rates. The high $m$ values were also expected since titanium is inherently good at retaining its strength at elevated temperatures and is less sensitive to thermal softening.

Table 4.12: J-C results from different machining direction vs. print (build) orientation.

| Direction | $A$ (MPa) | $B$ (MPa) | $n$ | $C$ | $m$ |
|---|---|---|---|---|---|
| AM VerXY1 | 1062 | 644.8 | 0.486 | 0.0553 | 1.905 |
| AM VerXY2 | 1062 | 644.8 | 0.486 | 0.0813 | 2.000 |
| AM VerZ | 1062 | 644.8 | 0.486 | 0.0679 | 1.998 |
| AM HorXY1 | 1093 | 690.8 | 0.389 | 0.0858 | 1.740 |
| AM HorXY2 | 1093 | 701.1 | 0.418 | 0.0713 | 2.000 |
| AM HorZ | 1093 | 777.8 | 0.372 | 0.0499 | 1.861 |
| Wrought | 1038 | 401.5 | 0.473 | 0.0475 | 1.621 |

The strain rate hardening (between 0.0475 to 0.0858) and thermal softening exponent (between 1.621 to 2.000) for titanium Ti-6Al-4V was much higher than those values found by Lesuer et al. [3] (0.012 for strain rate hardening and 0.8 for thermal softening exponent). It is expected that titanium Ti-6Al-4V would have high strength against high strain rate, good ability to resist thermal softening, and the high $C$ and $m$ values found in this study supports these expectations. However, it should be noted that these values might not be indicative of the exact $C$ and $m$ value of titanium, as the Oxley model assumes continuous chip formation. In addition, J-C model is more well suited for continuous chip modelling than segmented chips [55]. Machining titanium always produces serrated chips, which can affect the accuracy of force prediction and ultimately the accuracy of the predicted $C$ and $m$.

Regardless, cutting force prediction is used again to validate the effectiveness of the model. As shown in Fig. 4.8, four cutting directions with different feeds and speeds were assessed.

The data from these conditions were not used as reference data when searching for

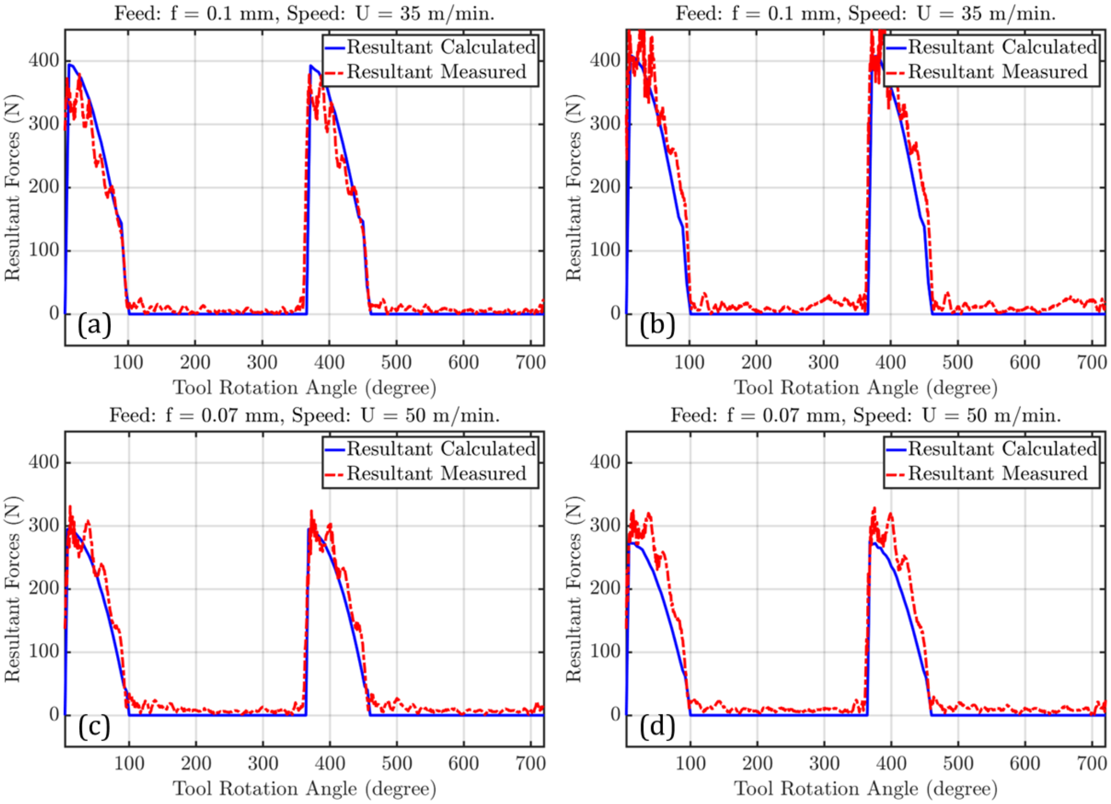

Figure 4.8: Calculated versus measured resultant forces at different feeds and speeds for (a) VerXY1, (b) VerZ, (c) HorXY1, and (d) HorZ. [4]

the J-C parameters. This allowed for an independent evaluation of the model's ability to predict cutting forces in novel situations. The results from all four of these cutting directions showed good agreement between the measured forces and calculated ones, indicating the generalizability and robustness of the model for a range of cutting conditions.

### 4.3.4 Characterizing the Mechanism of Chip Formation

During the machining of both wrought and AM titanium, saw-toothed chips were consistently observed for all cutting directions and a range of different feeds and speeds, as shown in Fig. 4.9. This is due to the phenomenon of adiabatic shear occurring within the primary shear zone. Adiabatic shear, also known as thermoplastic shear instability, is the result of the interaction between work hardening and thermal softening in the primary shear zone. When the strengthening effect of work hardening is offset by the gradients of local temperature in the primary shear zone, thermoplastic shear instability occurs, leading to the formation of segmented chips. This was particularly evident in the case of AM titanium, as it fundamentally inherits most of its property from wrought titanium, particularly its toughness, high work hardening and low thermal conductivity.

Machining both the vertically and horizontally printed block produced chips with clear and distinct shear bands. Although the shear band thickness of both AM and wrought titanium were almost similar, AM titanium shear bands appeared to be more pronounced. In addition, the shear bands in AM titanium penetrated deeper into the chip. The continuous flow thickness was 94 µm for wrought titanium chip, while it was only 68 µm and 54 µm for vertically and horizontally printed block, respectively. This was likely due to the increased hardness of AM titanium. Higher hardness dulls the cutting edge faster, leading to increased rubbing and more cutting power being directed towards generating heat rather than effectively shearing the workpiece material, exacerbating thermoplastic shear instability.

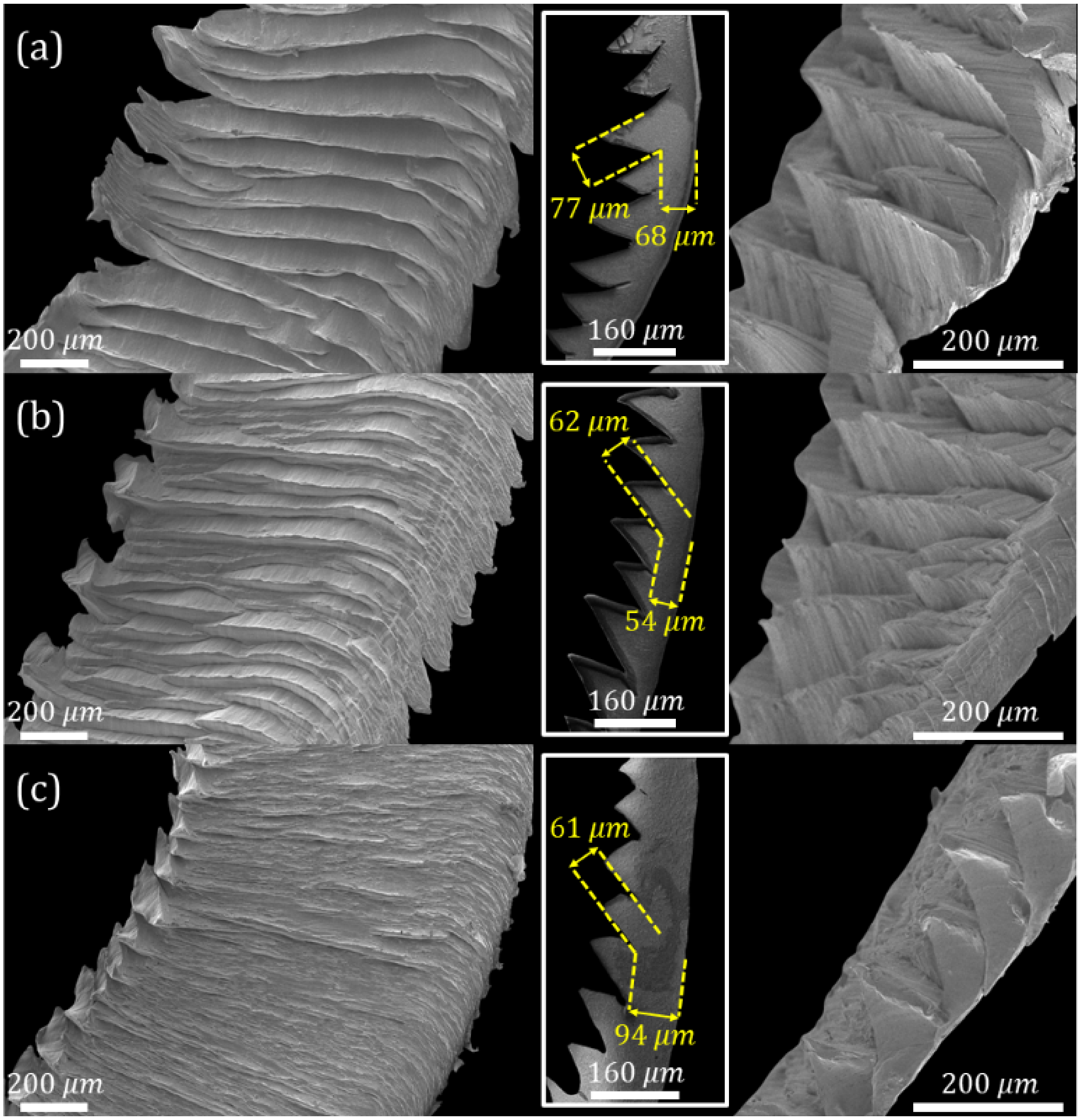

Figure 4.9: SEM images of chip produced by machining at feed and speed of 0.13 mm/tooth and 50 m/min on (a) vertically printed, (b) horizontally printed, and (c) wrought block. [4]

## 4.4 Summary

In this chapter, the results from experiments and tests on machining AISI 4340 hardened steel, Aluminum 6061-T6, and titanium Ti-6Al-4V are presented. The J-C parameters of the materials were determined using the proposed model. GA and PSO were tested to investigate the interchangeability of different optimization models. The reference forces for the J-C parameters were obtained from selected angular positions of the tool during one full rotation, with three different reference angles chosen to reduce the computational load on the algorithm. The results of the J-C parameter search showed good agreement with the values from open literature for AISI 4340 hardened steel, while the values for Aluminum 6061-T6 varied from the open literature due to unpredictable fluctuations in the cutting forces.

Tensile tests were carried out to evaluate the mechanical properties of titanium Ti-6Al-4V, with the J-C parameters obtained from the measured true stress-strain data. The results showed a difference in the ductility and ultimate strength between the wrought and AM specimens. The hardness of the AM titanium was found to be higher, leading to increased cutting forces during machining. The PSO method was used to determine the J-C parameters of the wrought and AM titanium, with the results showing good agreement between the predicted and measured cutting forces. The formation of saw-toothed chips during machining was observed, which is due to the phenomenon of adiabatic shear. The shear bands in the AM titanium were more pronounced and penetrated deeper into the chip due to the increased hardness of the material. The results demonstrate the effectiveness of the model in determining the J-C parameters and predicting cutting forces for a range of cutting conditions for different materials.

# Chapter 5

# Conclusion and Future Work

## 5.1 Conclusion

The Johnson Cook (J-C) constitutive material model is an important model capable of predicting the material behavior under high strain, strain rate, and temperature. This thesis presented a new method for determining these J-C parameters directly from end milling, as an oblique machining process. It offers a simple and efficient way of determining J-C parameters directly from any machining processes, overcoming the need for Split Hopkinson Pressure Bar test, custom-made tools for orthogonal turning tests, and measurement of final chip thickness.

Advantages of the proposed J-C determination method:

- The proposed method is based on a more realistic representation of general oblique machining processes compared to existing methods.
- It can be implemented with any search optimization algorithm, such as genetic algorithm.
- It is applicable to any metal, but the results are more accurate for materials

that exhibit continuous chip formation during the machining process, such as AISI 4340 hardened steel.

- Materials that produce discontinuous or serrated chips, such as titanium Ti-6Al-4V, can also be analyzed, but with caution as the Oxley model used in this method assumes continuous chips and stable machining scenarios.

Important considerations:

- The quality of the measured cutting forces is crucial as they are used as a reference for the J-C parameter search.
- If the measured cutting forces are obtained from unstable cutting conditions, the search results will be less accurate, ultimately leading to higher errors in predicting J-C parameters.

The results showed good agreement with the published values in the open literature for AISI 4340 hardened steel. The strain rate hardening was found to be between 0 and 0.0059, and the thermal softening exponent was found to be between 0.929 and 1.146, which are close to the results from open literature of 0.015 to 0.072 for strain rate hardening and 0.513 to 1.03 for thermal softening exponent. For Aluminum 6061-T6, the results varied from the values found in the open literature, 0.0994 to 0.1000 found in this thesis versus 0.002 found in open literature for strain rate hardening, and 1.893 to 2.000 found in this thesis versus 1.34 found in open literature. This discrepancy is likely due to the characteristic variations among batches produced by different vendors as well as unstable measured cutting forces. Both GA and PSO were able to converge to similar final J-C parameters, with PSO achieve approximately 5% better fitness score.

The mechanical properties of titanium Ti-6Al-4V were evaluated through tensile tests. A total of 9 tensile tests were performed, including specimens fabricated using the wrought method, specimens printed in the vertical orientation, and those printed in the horizontal orientation. The results showed that all 9 specimens demonstrated a similar behavior in the elastic region, but deviation was observed when entering the plastic region. The wrought Ti-6Al-4V specimens displayed the highest ductility, up to 19% elongation at break, compared to 13% for vertically printed samples, and only 8% for horizontally printed samples. The ultimate strength was found to be the highest in the vertically printed AM specimens, up to 1200 MPa. The hardness readings of the AM titanium were higher due to the AM process that increases the hardness and makes the material more brittle. All AM titanium samples have hardness of 48±0.5 HRC, while wrought titanium samples have lower hardness of 43±0.5 HRC. Due to the increased hardness, AM titanium was consistently observed to drive faster tool wear than wrought titanium. This faster tool wear leads to higher cutting forces and very prominent when machining titanium at higher cutting speed and feeds. An increased of approximately 30.8% in resultant cutting forces are observed when machining at 65 m/min for some AM machining tests. In contrast, the peak resultant cutting forces for wrought titanium are similar when increasing cutting speed from 35 m/min to 65 m/min. Cutting forces for wrought titanium only increases as feed increases.

The J-C parameters of wrought and AM titanium were obtained using PSO. The strain rate hardening coefficients are similar for all machining directions versus printing directions, ranging from 0.0553 to 0.813 for vertically printed titanium samples, and from 0.0499 to 0.0858 for horizontally printed samples. Similarly, the thermal softening exponent for all machining directions versus printing directions are also similar, ranging from 1.905 to 2.000 for vertically printed titanium samples, and from 1.740 to 2.000 for horizontally printed samples. The model was successful at predicting the required J-C parameters and showed good agreement between the measured forces and calculated ones in independent evaluations.

The found strain rate hardening and thermal softening exponent values indicated titanium's high strength against high strain rate and good ability to resist thermal softening. However, these values are much higher than those found in open literature. This discrepancy might be due to the usage of the extended thick shear zone Oxley model as the foundational cutting force prediction model. This model assumes stable continuous chips, but titanium produces saw-tooth chips even at low cutting speed. Finally, during the machining of both wrought and AM titanium, saw-toothed chips were consistently observed due to the phenomenon of adiabatic shear. The shear band thickness of both AM and wrought titanium was almost similar, but the shear bands in AM titanium appeared to be more pronounced and penetrated deeper into the chip due to the increased hardness of AM titanium.

## 5.2 Future Work

Future work related to the presented J-C material model parameters determination, cutting force prediction, and tool wear analysis can focus on the following:

1. Using the proposed model to expand the understanding of wider range of AM metals and materials, along with measure, report, and compare predictions on the cutting forces. Advanced AM materials includes cobalt chromium alloys such as Co-Cr-Mo [56], Al and Mg alloys such as Al-4.5Mg-0.66Sc-0.51Mn-0.37Zr, Ni or Co-based superalloys such as Inconel 625 and Inconel 718, intermetallic compounds such as Ti-48Al-2Mn-2Nb and Nb-22Si-26Ti-6Cr-3Hf-2Al, and metal matrix composites such as aluminum reinforced with aluminum borate whisker Al18B4O3 or nano-sized Al91Fe4Cr5 quasicrystal, Ti-6Al-4V reinforced with TiB or TiC, etc. [57].

2. Test the search result quality and speed of convergence of other optimization techniques, such as gradient-based optimization algorithms, to determine the most efficient algorithms for searching the unknown Oxley variables, as well as the unknown J-C parameters.

3. Utilize the proposed search method to predict the parameters of other material models, such as the Zerilli-Armstrong model and the Kocks–Mecking–Estrin model. Compare the accuracy of different models that take into account strain softening, which is important in accurate simulation of segmented chips.

4. Determine a better, more comprehensive machining model to either improve or take the place of Oxley model. This is due to the prominent effects of tool wear when machining AM metals, as well as AM materials typically being difficult to machine. Although Oxley model has good prediction capabilities, it is most suitable for predicting forces in machining process that produce continuous chips. Furthermore, the new model should be more efficient when predicting cutting forces. Current implemented Oxley model requires searching three unknown variables that takes a lot of computational effort, leading to long processing time for a prediction.

5. Develop a more comprehensive machining model to account for high rake angles, such as high helix end mills with helix angles of at least 60°. The current oblique model has only been tested with low rake angle of 5°. At higher rake angle, cutting forces along the X and Y axis might be significantly diverted to the Z axis. This will create a true universal predictive model for any arbitrary complex cutting tool.

6. Develop a force model that can include the effects of accelerated tool wear when machining AM materials. Enabling the use of optimization model to predict cutting speeds and feeds that maximize material removal rate while constraining

cutting forces to set values. This tool wear model could also predict final surface quality, which is important for post process finish machining of AM parts.

# References

[1] E.-G. Ng, T. I. El-Wardany, M. Dumitrescu, and M. A. Elbestawi, "Physics-based simulation of high speed machining," *Machining science and technology*, vol. 6, no. 3, pp. 301–329, 2002.

[2] N. Nguyen and A. Hosseini, "Direct calculation of johnson-cook constitutive material parameters for oblique cutting operations," *Journal of manufacturing processes*, vol. 92, pp. 226–237, 2023.

[3] D. R. Lesuer, G. J. Kay, and M. M. LeBlanc, "Modeling large-strain, high-rate deformation in metals," *Conference: Third Biennial Tri-Laboratory Engineering Conference on Modeling and Simulation*, July 2001.

[4] H. Kishawy, N. Nguyen, A. Hosseini, and M. Elbestawi, "Machining characteristics of additively manufactured titanium, cutting mechanics and chip morphology," *CIRP Annals - Manufacturing Technology*, 2023.

[5] ASTM, "Standard terminology for additive manufacturing technologies," Tech. Rep. F2792-12, American Society for Testing and Materials, West Conshohocken, PA, USA, 2012.

[6] A. Vafadar, F. Guzzomi, A. Rassau, and K. Hayward, "Advances in metal additive manufacturing: A review of common processes, industrial applications, and current challenges," *Applied sciences*, vol. 11, no. 3, pp. 1213–, 2021.

[7] J. Gonzalez-Gutierrez, S. Cano, S. Schuschnigg, C. Kukla, J. Sapkota, and C. Holzer, “Additive manufacturing of metallic and ceramic components by the material extrusion of highly-filled polymers: A review and future perspectives,” *Materials*, vol. 11, no. 5, pp. 840–, 2018.

[8] C. Suwanpreecha and A. Manonukul, “A review on material extrusion additive manufacturing of metal and how it compares with metal injection moulding,” *Metals (Basel)*, vol. 12, no. 3, pp. 429–, 2022.

[9] G. Singh, J.-M. Missiaen, D. Bouvard, and J.-M. Chaix, “Copper extrusion 3D printing using metal injection moulding feedstock: Analysis of process parameters for green density and surface roughness optimization,” *Additive manufacturing*, vol. 38, pp. 101778–, 2021.

[10] Z.-j. Tang, W.-w. Liu, Y.-w. Wang, K. M. Saleheen, Z.-c. Liu, S.-t. Peng, Z. Zhang, and H.-c. Zhang, “A review on in situ monitoring technology for directed energy deposition of metals,” *International journal of advanced manufacturing technology*, vol. 108, no. 11-12, pp. 3437–3463, 2020.

[11] A. Lores, N. Azurmendi, I. Agote, and E. Zuza, “A review on recent developments in binder jetting metal additive manufacturing: materials and process characteristics,” *Powder metallurgy*, vol. 62, no. 5, pp. 267–296, 2019.

[12] Y. L. Yap, C. Wang, S. L. Sing, V. Dikshit, W. Y. Yeong, and J. Wei, “Material jetting additive manufacturing: An experimental study using designed metrological benchmarks,” *Precision engineering*, vol. 50, pp. 275–285, 2017.

[13] A. Al Rashid, W. Ahmed, M. Y. Khalid, and M. Koç, “Vat photopolymerization of polymers and polymer composites: Processes and applications,” *Additive manufacturing*, vol. 47, pp. 102279–, 2021.

[14] Y. Zhang, L. Wu, X. Guo, S. Kane, Y. Deng, Y.-G. Jung, J.-H. Lee, and J. Zhang, "Additive manufacturing of metallic materials: A review," *Journal of Materials Engineering and Performance*, vol. 27, no. 1, pp. 1–13, 2018.

[15] D. Dev Singh, T. Mahender, and A. Raji Reddy, "Powder bed fusion process: A brief review," in *Materials today : proceedings*, vol. 46, pp. 350–355, Elsevier Ltd, 2021.

[16] J. R. Spaniol, "Design of a split hopkinson pressure bar facility for dynamic material characterization," *ProQuest Dissertations Publishing*, 2019.

[17] S. Nemat-Nasser, "Introduction to High Strain Rate Testing," in *Mechanical Testing and Evaluation*, vol. 8, pp. 427–428, ASM International, 01 2000.

[18] S. N. Melkote, W. Grzesik, J. Outeiro, J. Rech, V. Schulze, H. Attia, P.-J. Arrazola, R. M'Saoubi, and C. Saldana, "Advances in material and friction data for modelling of metal machining," *CIRP annals*, vol. 66, no. 2, pp. 731–754, 2017.

[19] J. Pegues, M. Roach, R. Scott Williamson, and N. Shamsaei, "Surface roughness effects on the fatigue strength of additively manufactured Ti-6Al-4V," *International journal of fatigue*, vol. 116, pp. 543–552, 2018.

[20] G. Rotella, S. Imbrogno, S. Candamano, and D. Umbrello, "Surface integrity of machined additively manufactured Ti alloys," *Journal of materials processing technology*, vol. 259, pp. 180–185, 2018.

[21] H. A. Kishawy and A. Hosseini, *Machining difficult-to-cut materials : basic principles and challenges.* Materials forming, machining and tribology, Cham, Switzerland: Springer, 2019.

[22] P. Guo, B. Zou, C. Huang, and H. Gao, "Study on microstructure, mechanical properties and machinability of efficiently additive manufactured aisi 316L stain-

less steel by high-power direct laser deposition," *Journal of materials processing technology*, vol. 240, pp. 12–22, 2017.

[23] G. Li, S. Chandra, R. A. Rahman Rashid, S. Palanisamy, and S. Ding, "Machinability of additively manufactured titanium alloys: A comprehensive review," *Journal of manufacturing processes*, vol. 75, pp. 72–99, 2022.

[24] R. Shivpuri, J. Hua, P. Mittal, A. Srivastava, and G. Lahoti, "Microstructure-mechanics interactions in modeling chip segmentation during titanium machining," *CIRP annals*, vol. 51, no. 1, pp. 71–74, 2002.

[25] D. Samantaray, S. Mandal, and A. Bhaduri, "A comparative study on johnson cook, modified zerilli–armstrong and arrhenius-type constitutive models to predict elevated temperature flow behaviour in modified 9cr–1mo steel," *Computational materials science*, vol. 47, no. 2, pp. 568–576, 2009.

[26] K. Hariharan and F. Barlat, "Modified kocks–mecking–estrin model to account nonlinear strain hardening," *Metallurgical and materials transactions. A, Physical metallurgy and materials science*, vol. 50, no. 2, pp. 513–517, 2019.

[27] G. R. Johnson, "A constitutive model and data for materials subjected to large strains, high strain rates, and high temperatures," *Proc. 7th Inf. Sympo. Ballistics*, pp. 541–547, 1983.

[28] F. Ducobu, E. Rivière-Lorphèvre, and E. Filippi, "Application of the coupled eulerian-lagrangian (cel) method to the modeling of orthogonal cutting," *European journal of mechanics, A, Solids*, vol. 59, pp. 58–66, 2016.

[29] W. K. Rule, "A numerical scheme for extracting strength model coefficients from taylor test data," *International journal of impact engineering*, vol. 19, no. 9, pp. 797–810, 1997.

[30] Y. Guo, “An integral method to determine the mechanical behavior of materials in metal cutting,” *Journal of materials processing technology*, vol. 142, no. 1, pp. 72–81, 2003.

[31] A. Manes, L. Peroni, M. Scapin, and M. Giglio, “Analysis of strain rate behavior of an al 6061 t6 alloy,” *Procedia Engineering*, vol. 10, pp. 3477–3482, 2011. 11th International Conference on the Mechanical Behavior of Materials (ICM11).

[32] W. Dabboussi and J. Nemes, “Modeling of ductile fracture using the dynamic punch test,” *International journal of mechanical sciences*, vol. 47, no. 8, pp. 1282–1299, 2005.

[33] A. Shrot and M. Bäker, “Determination of johnson–cook parameters from machining simulations,” *Computational materials science*, vol. 52, no. 1, pp. 298–304, 2012.

[34] L. Pang and H. A. Kishawy, “Modified Primary Shear Zone Analysis for Identification of Material Mechanical Behavior During Machining Process Using Genetic Algorithm,” *Journal of Manufacturing Science and Engineering*, vol. 134, 07 2012. 041003.

[35] C. Y. Seif, I. S. Hage, and R. F. Hamade, “Utilizing the drill cutting lip to extract johnson cook flow stress parameters for Al6061-T6,” *CIRP journal of manufacturing science and technology*, vol. 26, pp. 26–40, 2019.

[36] T. Özel and Y. Karpat, “Identification of constitutive material model parameters for high-strain rate metal cutting conditions using evolutionary computational algorithms,” *Materials and manufacturing processes*, vol. 22, no. 5, pp. 659–667, 2007.

[37] F. Klocke, D. Lung, and S. Buchkremer, “Inverse identification of the constitutive equation of inconel 718 and aisi 1045 from fe machining simulations,”

*Procedia CIRP*, vol. 8, pp. 212–217, 2013. 14th CIRP Conference on Modeling of Machining Operations (CIRP CMMO).

[38] P. Bosetti, M. Giorgio, and S. Bruschi, "Identification of johnson–cook and tresca's parameters for numerical modeling of aisi-304 machining processes," *Journal of Manufacturing Science and Engineering*, vol. 135, p. 051021, 10 2013.

[39] R. Franchi, A. Del Prete, and D. Umbrello, "Inverse analysis procedure to determine flow stress and friction data for finite element modeling of machining," *International journal of material forming*, vol. 10, no. 5, pp. 685–695, 2016.

[40] J. Ning and S. Liang, "Evaluation of an analytical model in the prediction of machining temperature of AISI 1045 steel and AISI 4340 steel," *Journal of Manufacturing and Materials Processing*, vol. 2, no. 4, pp. 74–, 2018.

[41] J. Ning, V. Nguyen, Y. Huang, K. T. Hartwig, and S. Y. Liang, "Inverse determination of Johnson–Cook model constants of ultra-fine-grained titanium based on chip formation model and iterative gradient search," *International journal of advanced manufacturing technology*, vol. 99, no. 5-8, pp. 1131–1140, 2018.

[42] M. Hardt, D. Schraknepper, and T. Bergs, "Investigations on the application of the downhill-simplex-algorithm to the inverse determination of material model parameters for FE-machining simulations," *Simulation modelling practice and theory*, vol. 107, pp. 102214–, 2021.

[43] R. Eisseler, D. Gutsche, C. Maucher, and H.-C. Möhring, "Inverse determination of Johnson-Cook parameters of additively produced anisotropic maraging steel," *Materials*, vol. 15, no. 1, pp. 26–, 2021.

[44] P. L. B. Oxley and M. C. Shaw, "Mechanics of Machining: An Analytical Approach to Assessing Machinability," *Journal of Applied Mechanics*, vol. 57, pp. 253–253, 03 1990.

[45] J. H. Holland, *Adaptation in natural and artificial systems : an introductory analysis with applications to biology, control, and artificial intelligence.* Complex adaptive systems, Cambridge, Mass: MIT Press, 1st mit press ed. ed., 1992.

[46] R. Eberhart and J. Kennedy, "A new optimizer using particle swarm theory," in *MHS'95. Proceedings of the Sixth International Symposium on Micro Machine and Human Science*, pp. 39–43, IEEE, 1995.

[47] L. Pang, A. Hosseini, H. Hussein, I. Deiab, and H. Kishawy, "Application of a new thick zone model to the cutting mechanics during end-milling," *International journal of mechanical sciences*, vol. 96-97, pp. 91–100, 2015.

[48] C. K. Sagar, T. Kumar, A. Priyadarshini, and A. K. Gupta, "Prediction and optimization of machining forces using oxley's predictive theory and RSM approach during machining of WHAs," *Defence technology*, vol. 15, no. 6, pp. 923–935, 2019.

[49] E. Budak, Y. Altintas¸, and E. J. A. Armarego, "Prediction of Milling Force Coefficients From Orthogonal Cutting Data," *Journal of Manufacturing Science and Engineering*, vol. 118, pp. 216–224, 05 1996.

[50] E. M. Trent and P. K. Wright, *Metal cutting.* Boston: Butterworth-Heinemann, 4th ed., 2000.

[51] B. Yilmaz, S. Karabulut, and A. Güllü, "A review of the chip breaking methods for continuous chips in turning," *Journal of manufacturing processes*, vol. 49, pp. 50–69, 2020.

[52] A. Hassanat, K. Almohammadi, E. Alkafaween, E. Abunawas, A. Hammouri, and V. B. S. Prasath, "Choosing mutation and crossover ratios for genetic algorithms—a review with a new dynamic approach," *Information (Basel)*, vol. 10, no. 12, pp. 390–, 2019.

[53] G. R. Johnson and W. H. Cook, "Fracture characteristics of three metals subjected to various strains, strain rates, temperatures and pressures," *Engineering Fracture Mechanics*, vol. 21, no. 1, pp. 31–48, 1985.

[54] H. Chandrasekaran, R. M'Saoubi, and H. Chazal, "Modelling of material flow stress in chip formation process from orthogonal milling and split hopkinson bar tests," *Machining science and technology*, vol. 9, no. 1, pp. 131–145, 2005.

[55] F. Ducobu, E. Rivière-Lorphèvre, and E. Filippi, "On the importance of the choice of the parameters of the johnson-cook constitutive model and their influence on the results of a ti6al4v orthogonal cutting model," *International journal of mechanical sciences*, vol. 122, pp. 143–155, 2017.

[56] S. Singh, S. Ramakrishna, and R. Singh, "Material issues in additive manufacturing: A review," *Journal of manufacturing processes*, vol. 25, pp. 185–200, 2017.

[57] N. Li, S. Huang, G. Zhang, R. Qin, W. Liu, H. Xiong, G. Shi, and J. Blackburn, "Progress in additive manufacturing on new materials: A review," *Journal of materials science and technology*, vol. 35, no. 2, pp. 242–269, 2019.